The Astrophysical Journal, 927:152 (24pp), 2022 March 10 https://doi.org/10.3847/1538-4357/ac4e94
© 2022. The Author(s). Published by the American Astronomical Society.
OPEN ACCESS

Physical Constraints on the Extended Interstellar Medium of the $z = 6.42$ Quasar J1148+5251: $[C\,II]_{158\,\mu m}$, $[N\,II]_{205\,\mu m}$, and $[O\,I]_{146\,\mu m}$ Observations

Romain A. Meyer[1], Fabian Walter[1], Claudia Cicone[2], Pierre Cox[3], Roberto Decarli[4], Roberto Neri[5], Mladen Novak[1], Antonio Pensabene[4], Dominik Riechers[6], and Axel Weiss[7]
[1] Max Planck Institute for Astronomy, Königstuhl 17, D-D-69117, Heidelberg, Germany; meyer@mpia.de
[2] Institute of Theoretical Astrophysics, University of Oslo, P.O. Box 1029, Blindern, NO-0315 Oslo, Norway
[3] Sorbonne Université, UPMC Université Paris 6 and CNRS, UMR 7095, Institut d'Astrophysique de Paris, 98bis Boulevard Arago, F-75014 Paris, France
[4] INAF—Osservatorio di Astrofisica e Scienza dello Spazio di Bologna, via Gobetti 93/3, I-40129, Bologna, Italy
[5] Institut de Radioastronomie Millimétrique (IRAM), 300 Rue de la Piscine, F-38400 Saint-Martin-d'Héres, France
[6] I. Physikalisches Institut, Universität zu Köln, Zülpicher Strasse 77, D-50937 Köln, Germany
[7] Max-Planck-Institut für Radioastronomie, Auf dem Hügel 71, D-53121 Bonn, Germany
Received 2021 July 6; revised 2021 October 6; accepted 2022 January 20; published 2022 March 11

Abstract

We report new Northern Extended Millimeter Array observations of the $[C\,II]_{158\,\mu m}$, $[N\,II]_{205\,\mu m}$, and $[O\,I]_{146\,\mu m}$ atomic fine structure lines (FSLs) and dust continuum emission of J1148+5251, a $z = 6.42$ quasar, which probe the physical properties of its interstellar medium (ISM). The radially averaged $[C\,II]_{158\,\mu m}$ and dust continuum emission have similar extensions (up to $\theta = 2.51^{+0.46}_{-0.25}$ arcsec, corresponding to $r = 9.8^{+3.3}_{-2.1}$ kpc, accounting for beam convolution), confirming that J1148+5251 is the quasar with the largest $[C\,II]_{158\,\mu m}$-emitting reservoir known at these epochs. Moreover, if the $[C\,II]_{158\,\mu m}$ emission is examined only along its NE–SW axis, a significant excess ($>5.8\sigma$) of $[C\,II]_{158\,\mu m}$ emission (with respect to the dust) is detected. The new wide-bandwidth observations enable us to accurately constrain the continuum emission, and do not statistically require the presence of broad $[C\,II]_{158\,\mu m}$ line wings that were reported in previous studies. We also report the first detection of the $[O\,I]_{146\,\mu m}$ and (tentatively) $[N\,II]_{205\,\mu m}$ emission lines in J1148+5251. Using FSL ratios of the $[C\,II]_{158\,\mu m}$, $[N\,II]_{205\,\mu m}$, $[O\,I]_{146\,\mu m}$, and previously measured $[C\,I]_{369\,\mu m}$ emission lines, we show that J1148+5251 has similar ISM conditions compared to lower-redshift (ultra)luminous infrared galaxies. CLOUDY modeling of the FSL ratios excludes X-ray-dominated regions and favors photodissociation regions as the origin of the FSL emission. We find that a high radiation field ($10^{3.5-4.5}\,G_0$), a high gas density ($n \simeq 10^{3.5-4.5}$ cm^{-3}), and an H I column density of 10^{23} cm^{-2} reproduce the observed FSL ratios well.

Unified Astronomy Thesaurus concepts: Quasars (1319); High-redshift galaxies (734); Interstellar medium (847); Interferometry (808); Millimeter astronomy (1061)

1. Introduction

Luminous quasar activity is a key process of galaxy evolution. Indeed, massive outflows driven by the radiation pressure generated by the accretion of gas onto the central supermassive black hole (SMBH) or so-called "Active Galactic Nuclei (AGNs) feedback" are invoked in most models of galaxy formation to clear massive galaxies of their gas and quench star formation (e.g., Silk & Rees 1998; Di Matteo et al. 2005; Springel et al. 2005; King 2010; Costa et al. 2014; Ishibashi & Fabian 2015; Richardson et al. 2016; Negri & Volonteri 2017; Oppenheimer et al. 2020; Koudmani et al. 2021). Luminous quasars are most interesting at high redshift in particular, when they probe the early phase of coevolution between the first galaxies and their central black hole. The advent of large optical and infrared surveys has enabled the discovery of quasars up to $z \sim 7.5$ (Bañados et al. 2018; Yang et al. 2020; Wang et al. 2021), with several hundreds at $z > 6$ (see Bosman 2020 for an up-to-date list). These early quasars harbor SMBHs with $M_\bullet \gtrsim 10^8\,M_\odot$ and accrete gas at or near the Eddington limit for most of their life, challenging models of SMBH formation and growth (e.g., De Rosa et al. 2014; Mazzucchelli et al. 2017; Bañados et al. 2018; Wang et al. 2021). Because the bright quasar light outshines that of the host in the optical and near-infrared, the galaxies hosting early luminous quasars remained relatively mysterious until the advent of modern (sub)millimeter observatories.

Numerous observations of $z > 6$ quasars targeting the bright far-infrared (FIR) $[C\,II]_{158\,\mu m}$ emission line have revealed their host galaxies to be infrared luminous, dusty, and actively forming stars with estimated rates of 10^2–$10^3 M_\odot$yr^{-1} (e.g., Walter et al. 2003, 2009a; Maiolino et al. 2005, 2012; Wang et al. 2013, 2019; Bañados et al. 2015; Decarli et al. 2018; Venemans et al. 2018, 2020; Novak et al. 2019, 2020; Yang et al. 2020). $[C\,II]_{158\,\mu m}$ kinematics also show that most quasar hosts are massive galaxies ($M_* \sim 10^{10}\,M_\odot$) displaying a variety of morphologies, such as stable disks, bulge-dominated galaxies, and mergers with nearby companions (Wang et al. 2013, 2019; Shao et al. 2017, 2019; Decarli et al. 2019a, 2019b; Neeleman et al. 2019, 2021). The reports of broad $[C\,II]_{158\,\mu m}$ line wings in the $z = 6.42$ quasar J1148+5251 (Maiolino et al. 2012; Cicone et al. 2015) spurred the use of the $[C\,II]_{158\,\mu m}$ emission line to identify quasar outflow signatures in the early universe. Such features have remained rare, however, and stacking analyses have led to contradictory results (Bischetti et al. 2019; Novak et al. 2020). Recently, Izumi et al. (2021a, 2021b) reported broad $[C\,II]_{158\,\mu m}$ line wings in two low-luminosity quasars at $z = 6.72$ and $z = 7.07$.

Original content from this work may be used under the terms of the Creative Commons Attribution 4.0 licence. Any further distribution of this work must maintain attribution to the author(s) and the title of the work, journal citation and DOI.

Two decades of [C II]$_{158\ \mu m}$ and CO studies have shown that early luminous quasars provide an unparalleled observational window into the physics of the earliest (and most massive) galaxies in the universe. However, multiline studies using lines other than [C II]$_{158\ \mu m}$ and CO transitions have been much rarer until now. Since different fine structure lines (FSLs) trace different gas densities and excitation levels, only in combination can they probe the ionized and neutral atomic gas phases, and the excitation source(s) of the gas (see, e.g., Carilli & Walter 2013 for a review). Besides [C II]$_{158\ \mu m}$, potential atomic FSLs of interest include [N II]$_{122\ \mu m}$, [N II]$_{205\ \mu m}$, [O I]$_{63\ \mu m}$, [O I]$_{145\ \mu m}$, [O III]$_{88\ \mu m}$, and [C I]$_{369\ \mu m}$, all accessible at $z \sim 6$ with (sub)millimeter arrays such as the Atacama Large Millimeter Array or the Northern Extended Millimeter Array (NOEMA). Moreover, these lines have been observed with Herschel in large samples of local (ultra)luminous infrared galaxies—or (U)LIRGs—which can be readily compared to $z \sim 6$ quasar hosts (e.g., Díaz-Santos et al. 2017; Herrera-Camus et al. 2018a).

Detections of FSLs other than [C II]$_{158\ \mu m}$ in $z > 6$ quasars are still relatively recent (Walter et al. 2018; Hashimoto et al. 2019; Novak et al. 2019; Li et al. 2020), and a complex picture is emerging from these first results. Emission lines probing the neutral phase ([O I]$_{145\ \mu m}$ and [C I]$_{369\ \mu m}$) show good agreement between the line ratios and line-to-FIR ratios of distant quasars and local (U)LIRGs (Novak et al. 2019; Li et al. 2020). While Novak et al. (2019) and Li et al. (2020) report potentially high [O III]$_{88\ \mu m}$ to [C II]$_{158\ \mu m}$ ratios ($\sim$2) in J1342+0928 and J2310+1855, respectively, this is not the case for the quasar J2100–1715 and its companion galaxy (Walter et al. 2018), which have ratios similar to the average of the local population of LIRGS and AGNs ($\sim$0.1–1; Herrera-Camus et al. 2018a). These first results are difficult to interpret, however, since the origins of FSLs are not always clearly determined, and can be linked to different phases (as is the case for the [C II]$_{158\ \mu m}$ emission line). Clearly, more FIR multiline studies of $z > 6$ quasars are needed to understand the interstellar medium (ISM) of their host galaxies.

SDSS J1148+5251 is one of the earliest high-redshift quasars discovered in the Sloan Digital Sky Survey (SDSS; Fan et al. 2003; $z = 6.4189$), and harbors a $3 \times 10^9 M_\odot$ SMBH (Willott et al. 2003). Being the redshift record holder for many years after its discovery, it was extensively observed with the Very Large Array and the IRAM Plateau de Bure Interferometer (PdBI), and was the first object detected in CO and [C II]$_{158\ \mu m}$ at $z > 5$ (Bertoldi et al. 2003b, 2003a; Walter et al. 2003, 2004, 2009a, 2009b; Maiolino et al. 2005; Riechers et al. 2009). These pioneering studies probed the host galaxy star formation rate (SFR), dust, and ISM properties. Additionally, Maiolino et al. (2012) and Cicone et al. (2015) reported the presence of a broad [C II]$_{158\ \mu m}$ emission ($\sigma_v = 900$ km s^{-1}) component in the PdBI data, suggesting the presence of an outflow as well as spatially extended [C II]$_{158\ \mu m}$ emission (up to $r \sim 30$ kpc). In this paper, we return to J1148+5251 with a new set of NOEMA observations, capitalizing on larger bandwidths and more antennas, thus improving on the image fidelity as compared to earlier PdBI observations. The new observations targeted atomic FSLs ([O I]$_{146\ \mu m}$, [N II]$_{205\ \mu m}$) and other molecular (CO, H_2O) rotational transitions. The aim of the observations was to dissect the ISM phases without relying on assumptions about the origin of [C II]$_{158\ \mu m}$ that can come from both the ionized and neutral phases. Indeed, [O I]$_{146\ \mu m}$ traces exclusively the neutral phase/photodissociated regions (PDRs), whereas [N II]$_{205\ \mu m}$ traces the ionized/H II regions. This set of observations is complemented with earlier [C I]$_{369\ \mu m}$ data (Riechers et al. 2009) that trace the neutral/molecular gas. Thanks to the wide spectral coverage of the new NOEMA correlator *PolyFix* and the upgraded NOEMA array, these observations achieved a high fidelity that resulted in deep [C II]$_{158\ \mu m}$ observations and tight constraints on the underlying dust continuum.

The structure of this paper is as follows. We present in Sections 2 and 3 the new observations of the [C II]$_{158\ \mu m}$, [N II]$_{205\ \mu m}$, and [O I]$_{146\ \mu m}$ emission lines in J1148+5251, as well as the FIR continuum observed between 200 and 280 GHz. We focus on the [C II]$_{158\ \mu m}$ emission line to reassess the evidence for a broad velocity component and investigate its spatial extension in Section 4. In Section 5, we derive ISM properties from the strength of the atomic FSLs observed, before concluding our study in Section 6. Throughout this paper, we assume a concordance cosmology with $H_0 = 70$ km s^{-1}Mpc^{-1}, $\Omega_M = 0.3$, and $\Omega_\Lambda = 0.7$. At the redshift of the target ($z = 6.42$), $1''$ corresponds to 5.62 proper kpc.

2. Observations and Data Reduction

We have observed the $z = 6.4189$ quasar J1148+5251 using NOEMA (Project ID: w17ex001/w17ex001; PI: F. Walter). The pointing and phase center of our observations were chosen to correspond to the quasar position in the optical SDSS imaging (R.A. = 11:48:16.64, decl. = +52:51:50.32). The observations included two spectral setups taking advantage of the new *PolyFix* correlator, covering simultaneously two 7.744 GHz wide sidebands.[8] The first spectral setup was centered at 267 GHz, such that the lower sideband (255–263 GHz) covers the redshifted [C II]$_{158\ \mu m}$ emission with one sideband, while the upper sideband (271–279 GHz) covers the [O I]$_{146\ \mu m}$ emission. The second setup was centered at 208 GHz to cover the [N II]$_{205\ \mu m}$ in the lower sideband (196–204 GHz). The setups also covered two high-J CO (14–13 and 13–12) and H_2O rotational transitions ($5_{23} - 4_{32}$ and $3_{22} - 3_{13}$), which will be discussed in future works. The observations were executed between 2017 December and 2018 May. The [C II]$_{158\ \mu m}$ and [O I]$_{146\ \mu m}$ setup was mostly observed in configuration 9D, except for two tracks using eight antennas (with baselines ranging from 24 to 176 m), for a total observing time of 18.7 hr. Data was (remotely) reduced at IRAM Grenoble using the *CLIC* package within the GILDAS framework (jan2021a version).[9] We reach an rms noise of 0.64(0.88) mJy beam^{-1} in 50 km s^{-1} channels, and the synthesized beam FWHM size is $1\farcs97 \times 1\farcs59$ ($1\farcs83 \times 1\farcs51$) for the [C II]$_{158\ \mu m}$([O I]$_{146\ \mu m}$) line observations. The [N II]$_{205\ \mu m}$ and CO lines were observed with eight antennas for a total of 15.7 hr, with baselines ranging from 24 to 176 m. For the [N II]$_{205\ \mu m}$ line, the noise rms is 0.78 mJy beam^{-1} in 50 km s^{-1} channels, and the synthesized beam size $1\farcs79 \times 1\farcs51$. For the continuum, the synthesized beam size achieved is $1\farcs78 \times 1\farcs51$, $1\farcs65 \times 1\farcs46$, $1\farcs91 \times 1\farcs71$, and $1\farcs88 \times 1\farcs52$ at 200, 212, 259, and 272 GHz, respectively.

Imaging and cleaning was performed using the latest version of MAPPING/GILDAS (jan2021a). The dirty maps were obtained from the visibilities without tapering and using natural weighting. The data were not primary beam–corrected.[10]

[8] https://www.iram-institute.org/EN/content-page-96-7-56-96-0-0.html

[9] https://www.iram.fr/~gildas/dist/

[10] As the source is located at the phase center, even at the edge of the aperture considered in the analysis ($r = 3''$) the correction is minimal (1.06) and does not impact the results.

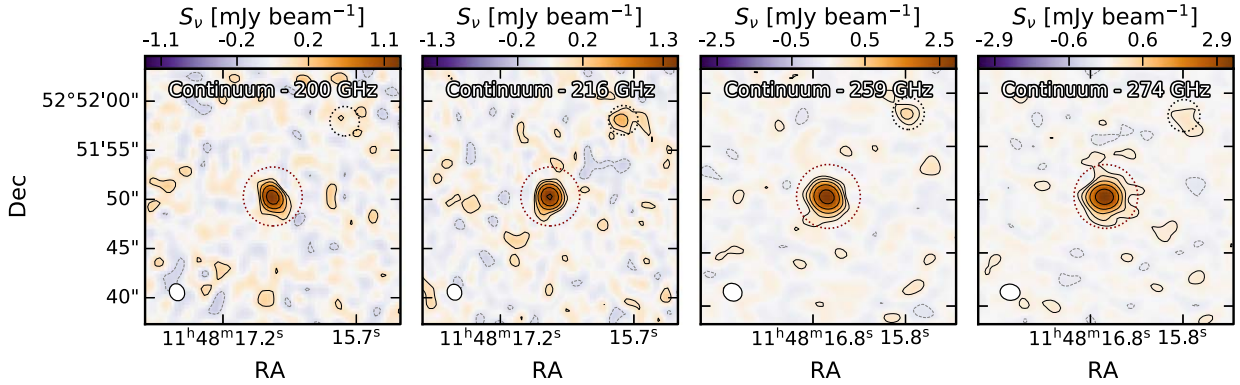


Figure 1. Dust continuum emission maps integrated over the ∼7.68 GHz effective bandwidth of the Polyfix correlator for each sideband, with central frequencies 200, 216, 259, and 274 GHz. The dotted circle centered on J1148+5251 indicates the aperture radius of 3″ adopted throughout this paper for flux density estimates. An additional source, reported previously by Leipski et al. (2010) and Cicone et al. (2015), is visible to the NW in the three higher-frequency bands at ∼10″ (the black dotted circle). The contours are logarithmic (− 4, − 2, 2, 4, 8, 16, 32)σ (rms). The color scaling is log-linear, the threshold being at 3σ.

Cleaning was performed down to 2σ (where σ is the rms noise in the dirty map) using a circular clean region of radius $r = 5''$. The reason for choosing such a wide radius was the earlier reports of extended [C II]$_{158\ \mu m}$ emission (Maiolino et al. 2012; Cicone et al. 2015). An additional clean region with radius $r = 2''$ was added on the NW source reported by Leipski et al. (2010) and Cicone et al. (2015), which is also detected in the NOEMA data.[11] The final products were created using the following procedure. First, data cubes with 50 km s^{-1} channels were produced to search for significant emission lines. The [C II]$_{158\ \mu m}$, [N II]$_{205\ \mu m}$, [O I]$_{146\ \mu m}$, H_2O ($5_{23} - 4_{32}$ and $3_{22} - 3_{13}$, $\nu_{rest} = 258.7$ GHz), CO(14–13), and CO(13–12) emission lines were fitted with a single-Gaussian profile in order to estimate their FWHM. Continuum maps were created using all channels at least 1.25 × FWHM away from each emission line. The continuum, determined from the line-free channels using an order 1 interpolation (GILDAS *UV_BASELINE* routine) over the ∼7.6 GHz sidebands, was subtracted in the *uv* plane to create continuum-subtracted cubes.

In order to determine the significance of emission lines, velocity-integrated emission line maps ("line maps") were created by integrating channels over 1.2 times the FWHM of the [C II]$_{158\ \mu m}$ line (i.e., 482 km s^{-1}) at the redshifted frequency of the line. We use the [C II]$_{158\ \mu m}$ redshift ($z = 6.4189$) to determine the redshifted frequency of all lines. Such maps, assuming the line is Gaussian, contain by definition 84% of the total flux[12] (for a short derivation, see Appendix A of Novak et al. 2020). All of the total line fluxes measured from the line maps and reported in this paper account for this effect. Additionally, all continuum and line fluxes in this paper were computed using the residual scaling method (e.g., Jorsater & van Moorsel 1995; Walter & Brinks 1999; Walter et al. 2008; Novak et al. 2019).

In order to determine the aperture needed to recover most of the flux of the emission lines and the dust continuum, a curve of growth approach was adopted. We show in Appendix A that all line and continuum fluxes reach a maximum or plateau at an aperture radius $r = 3''$, which corresponds to 16.9 kpc at $z = 6.42$. A nominal aperture radius of 3″ is thus adopted throughout the paper. The line subtraction procedure described above was repeated using the $r = 3''$ aperture to obtain the final data cubes. Additionally, we investigate the use of multiscale cleaning in Appendix B. We conclude that the [C II]$_{158\ \mu m}$ emission and the 259–272 GHz continuum are better recovered using multiscale cleaning, and we therefore use multiscale cleaning with Gildas/MAPPING for these data throughout the paper.

Table 1
Continuum Measurements at 200–274 GHz Extracted from the Continuum Images (Figure 1, Effective Bandwidth ≃7.68 GHz (Masking the Edges and Central Baseband Gap) and Integrated in a Circular Aperture with Radius $r = 3''$)

ν_{obs} (GHz)	S_ν (mJy)	Rms (mJy)	Beam Size
200	1.78 ± 0.23	0.06	1.″78 × 1.″51
216	2.33 ± 0.21	0.05	1.″65 × 1.″46
259	4.64 ± 0.26	0.08	1.″91 × 1.″71
274	5.85 ± 0.29	0.08	1.″88 × 1.″52

3. Results

3.1. Dust Continuum Emission

We first present the FIR continuum maps in Figure 1. The FIR continuum is clearly detected in all four sidebands. The measured continuum flux densities are tabulated in Table 1. Due to the upgraded bandwidth of the NOEMA *PolyFix* correlator, these continuum measurements have higher sensitivity than previous observations at ∼260 GHz (Walter et al. 2009a; Maiolino et al. 2012; Cicone et al. 2015). The new continuum flux density at 259 GHz (4.64 ± 0.26 mJy) is in good agreement[13] with the earlier PdBI measurement from Walter et al. (2009a) and the 1.2 mm continuum measurement (5.0 ± 0.6 mJy; Bertoldi et al. 2003a). We combine our new continuum measurements with previous literature results at different frequencies (Bertoldi et al. 2003b; Walter et al. 2003; Robson et al. 2004; Riechers et al. 2009; Leipski et al. 2010;

[11] We found no emission lines for this source in any of the spectral setups used in this work.

[12] We have checked that this correction holds for the [C II]$_{158\ \mu m}$ emission, where the flux recovered in a (−1500, +1500) km s^{-1} velocity-integrated map is $S_{line}\Delta v = 10.5 \pm 0.92$ Jy km s^{-1}, and the 1/0.84-corrected flux in the nominal 1.2 × FWHM$_{[C\ II]}$ = 482 km s^{-1} channel is $S_{line}\Delta v = 10.4 \pm 0.5$ Jy km s^{-1}, where S_{line} is integrated in a circular aperture with $r = 3''$. Indeed, the choice of a 1.2× FWHM-wide channel maximizes the signal-to-noise ratio without flux losses.

[13] We have checked that there is no continuum offset between the two sidebands by imaging the calibrators (1150+497 and 1216+487) for every track and the stacked data.

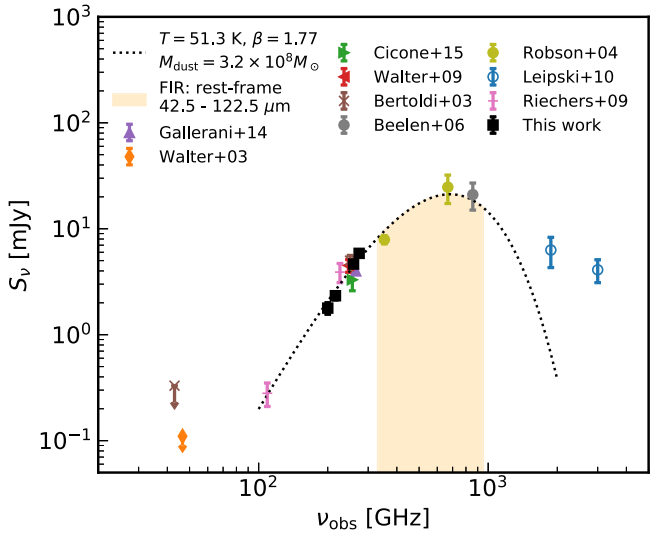


Figure 2. Continuum measurements from the literature and this work with the best-fit modified blackbody dust emission model. The effect of the CMB is accounted for as prescribed by Da Cunha et al. (2013), and the data points at $\nu > 10^3$ GHz are not used for the fit. The FIR luminosity, integrated over the shaded orange area, is not significantly affected by this choice.

Gallerani et al. 2014) to fit the FIR spectral energy distribution (SED).

Assuming optically thin dust emission at $\lambda > 40$ μm (e.g., Beelen et al. 2006), we use a modified blackbody model for the dust emission and correct both for contrast and cosmic microwave background (CMB) heating, as prescribed by Da Cunha et al. (2013). The dust mass is derived assuming an opacity $\kappa_{\nu_{\rm rest}} = \kappa_{\nu_0}(\nu_{\rm rest}/\nu_0)^\beta$, with $\nu_0 = c/(125\ \mu{\rm m})$ and $\kappa_0 = 2.64\ {\rm m^2\ kg^{-1}}$, following Dunne et al. (2003), with β being the dust spectral emissivity index. Our purpose is primarily to measure the FIR luminosity to constrain the SFR in J1148+5251. Therefore, we omit data points at $\nu_{\rm rest} > 1000$ GHz ($\lambda_{\rm rest} \lesssim 125$ μm), where contamination by the quasar nonthermal and torus emission becomes significant (e.g., Leipski et al. 2010, 2014). The dust SED model uses three free parameters (total dust mass M_d, dust emissivity index β, and dust temperature T_d) and is fitted using a Markov Chain Monte Carlo with the *emcee* package (Foreman-Mackey et al. 2013). The resulting best-fit and observational constraints are shown in Figure 2, and the posterior probability distribution of the dust SED parameters is displayed in Appendix C. The median dust mass is $3.2 \times 10^8 M_\odot$, the median dust SED index is $\beta = 1.77^{+0.30}_{-0.26}$, and the median dust temperature is moderately high ($T_d = 51.3$ K), in agreement with earlier studies (e.g., Beelen et al. 2006; Leipski et al. 2010; Cicone et al. 2015), which is not surprising, considering that most of the constraining power comes from observations at lower and higher frequencies than those reported in this work.

We integrate the modified blackbody to derive the total infrared (IR; 8–1000 μm) and FIR (42.5–122.5 μm; e.g., Helou et al. 1985) luminosities. The total IR luminosity is $L_{\rm IR} = (20.9 \pm 6.8) \times 10^{12} L_\odot$ and the FIR luminosity $L_{\rm FIR} = (13.4 \pm 2.4) \times 10^{12} L_\odot$, in agreement with earlier studies of J1148+5251. Assuming that dust heating is dominated by young stars, the IR luminosity can be converted to an SFR using the Kennicutt (1998) and Kennicutt & Evans (2012) conversions, giving ${\rm SFR} = (1830 \pm 595) - (2090 \pm 680) M_\odot\ {\rm yr^{-1}}$, respectively. This is in agreement with earlier studies that found that J1148+5251 is in an intense starburst phase (Maiolino et al. 2005, 2012; Walter et al. 2009a; Cicone et al. 2015).

3.2. FSL Detections

We present the line maps for the [C II]$_{158\ \mu{\rm m}}$, [O I]$_{146\ \mu{\rm m}}$, and [N II]$_{205\ \mu{\rm m}}$ emission in Figure 3. For comparison, we also show maps of the same channel width (482 km s^{-1}) as the main line map, but offset by ± 482 km s^{-1} from the line emission, to visually assess the robustness of our detections. The spectra of the [C II]$_{158\ \mu{\rm m}}$ line are presented in Figure 5 (see also Appendix D), while the [O I]$_{146\ \mu{\rm m}}$ and [N II]$_{205\ \mu{\rm m}}$ spectra are shown in Figure 4.

We detect [C II]$_{158\ \mu{\rm m}}$ and [O I]$_{146\ \mu{\rm m}}$ at 42σ and 5.3σ (where the signal-to-noise ratio (S/N) is calculated using the peak surface brightness in the line maps and the pixel rms level). [N II]$_{205\ \mu{\rm m}}$ is only marginally detected (3.7σ), and its peak emission is potentially offset from the rest-frame UV, dust, [C II]$_{158\ \mu{\rm m}}$, and [O I]$_{146\ \mu{\rm m}}$ emission. In the central pixel of the [C II]$_{158\ \mu{\rm m}}$ emission, [N II]$_{205\ \mu{\rm m}}$ is formally undetected. We defer further discussion of the [N II]$_{205\ \mu{\rm m}}$ emission line to Section 5.2. In our subsequent analysis of the ISM of J1148+5251, we focus on the extended aperture-integrated fluxes. All of the fluxes and derived line luminosities are tabulated in Table 2. For comparison, we have also measured the flux density of the [C II]$_{158\ \mu{\rm m}}$ emission by fitting the aperture-integrated spectrum with a Gaussian, and we show a comparison between our work and earlier studies for various aperture sizes in Appendix D. In summary, we find a good agreement between the line map flux estimates and the spectrum best-fit values, as well as good agreement between previous studies and the data presented here, as long as the "core" ($<3''$ emission, with no velocity offsets) [C II]$_{158\ \mu{\rm m}}$ emission is considered.

4. The Spatial and Velocity Structure of the [C II]$_{158\ \mu{\rm m}}$ Emission in J1148+5251

4.1. Spectral Analysis

Figure 5 shows the total and continuum-subtracted [C II]$_{158\ \mu{\rm m}}$ spectra (extracted in an $r = 3''$ aperture), as well as single- and double-Gaussian fits to the data. We found an emission feature at 262.2 GHz that was subsequently masked to determine and subtract the continuum. An emission line map of the feature does not reveal any convincing emission, and we are not aware of any strong molecular or ionized line that could correspond to this redshifted frequency. We checked that masking this feature or not marking it does not impact any of the results that follow. We find that a single Gaussian describes the [C II]$_{158\ \mu{\rm m}}$ emission well, both in the total and continuum-subtracted spectra, and that the single-Gaussian residuals are consistent with the rms noise (Figure 5). For the total spectrum, the best-fit single-Gaussian and continuum model has a monochromatic continuum flux density of $S_\nu = 4.6 \pm 0.2$ mJy, [C II]$_{158\ \mu{\rm m}}$ observed frequency $\nu_{\rm [C\ II],obs} = 256.158 \pm 0.008$ GHz, [C II]$_{158\ \mu{\rm m}}$ FWHM $= 408 \pm 23$ km s^{-1}, and integrated flux $I_\nu = 10.0 \pm 0.8$ Jy km s^{-1}. The best-fit double-Gaussian and continuum model has a continuum flux density of $S_\nu = 4.5 \pm 0.2$ mJy, $\nu^{\rm narrow}_{\rm [C\ II],obs} = 256.159 \pm 0.009$ GHz, [C II]$_{158\ \mu{\rm m}}$ FWHM$^{\rm narrow} = 373 \pm 36$ km s^{-1}, and narrow-component integrated flux $I_\nu^{\rm narrow} = 8.7 \pm 1.0$ Jy km s^{-1}. The broad component has a central frequency $\nu^{\rm broad}_{\rm [C\ II],obs} = 256.19 \pm 0.20$ GHz, [C II]$_{158\ \mu{\rm m}}$ FWHM$^{\rm broad} = 1330 \pm 820$ km s^{-1}, and integrated flux $I_\nu^{\rm broad} = 2.9 \pm 3.0$ Jy km s^{-1}. The χ^2 difference between the single- and double-Gaussian models is only $\Delta\chi^2 = 3.66$ for three additional degrees of freedom, which corresponds to a p-value of $p = 0.7$ or evidence at the 0.52σ level for a broad component. Equivalently, the Bayesian Information Criterion (BIC) difference is ${\rm BIC}_1 -$

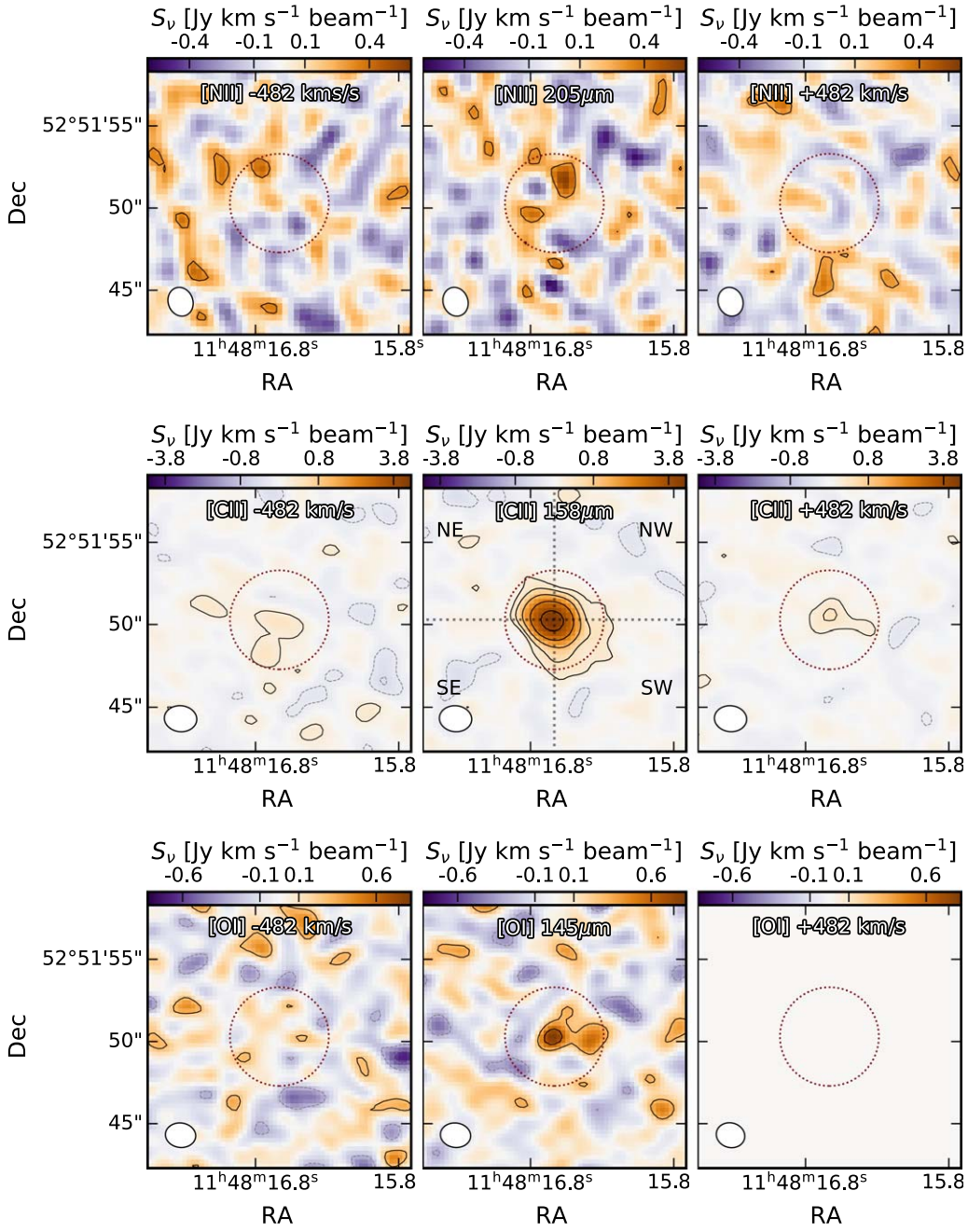


Figure 3. Line maps, velocity-integrated over $1.2 \times \mathrm{FWHM}_{[\mathrm{C\,II}]} = 482$ km s^{-1} at the expected frequencies of [C II]$_{158\ \mu\mathrm{m}}$, [N II]$_{205\ \mu\mathrm{m}}$, and [O I]$_{146\ \mu\mathrm{m}}$, and assuming the [C II]$_{158\ \mu\mathrm{m}}$ redshift. For each line, we also plot two additional collapsed maps, centered at $\pm$ 482 km s^{-1} away from the line emission. For [O I]$_{146\ \mu\mathrm{m}}$, only one of the adjacent maps is empty, as the emission is at the edge of the band. On the central [C II]$_{158\ \mu\mathrm{m}}$ map, we plot the quadrants used for the spatial extension analysis in Section 4.2. The contours are logarithmic (-4, -2, 2, 4, 8, 16, 32)σ (rms).

$\mathrm{BIC}_2 = -12.0$, where a lower BIC implies a better model, and we adopt a threshold $\Delta\mathrm{BIC}_{12} > 10$ for strong significance to prefer the more complex model (e.g., Kass & Raftery 1995). We also perform an Anderson–Darling test on the residuals to find any deviations from normally distributed residuals (with a variance equal to the measured rms squared). We find no significant deviation, for either fit, at the $p > 0.15$ level. We thus do not find evidence for a broad spectral [C II]$_{158\ \mu\mathrm{m}}$ component in J1148+5251 based on the new NOEMA data alone.

For the continuum-subtracted spectrum, the best-fit single- and double-Gaussian models yield consistent results within the uncertainties (for more details, including the impact of different aperture sizes, see Appendix D), and the residuals are nearly identical (Figure 5, second row, lower right). The χ^2 improvement obtained with a double Gaussian is $\Delta\chi^2 = 2.24$, which for an increase of three free parameters gives a p-value of 0.46 for rejecting the simple model in favor of a double Gaussian, in agreement with the analysis of the total spectrum. The BIC

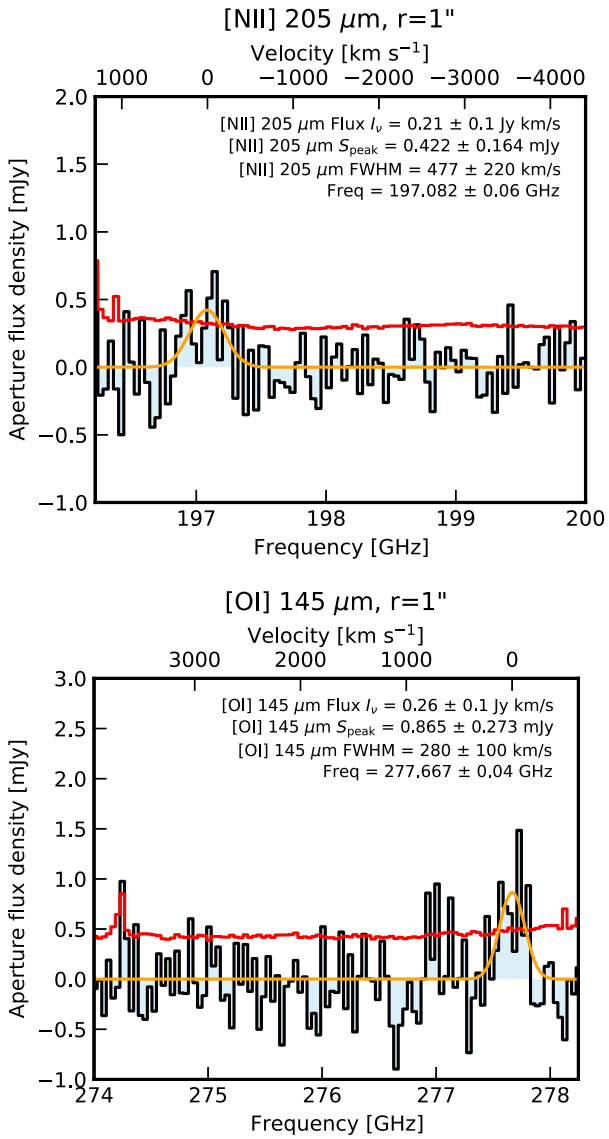


Figure 4. Continuum-subtracted spectrum of the [N II]$_{205\ \mu m}$ (upper panel) and [O I]$_{146\ \mu m}$ (lower panel). The spectra (black lines, shaded blue) are extracted in $r = 1''$ apertures centered on the peak of the emission in the velocity-integrated maps (Figure 3) using residual scaling (see Section 2). The 1σ noise level per channel for an $r = 1''$ aperture is shown in red, and a single-Gaussian fit is shown in orange (the best-fit parameters and uncertainties are in the upper right corners).

difference is $BIC_1 - BIC_2 = -14.0$, e.g., the single-Gaussian model is strongly favored, and an Anderson–Darling test on the residuals also concludes that they are consistent with the measured noise at the $p > 0.15$ level.

We note that, regardless of the aperture chosen or the use of residual scaling, the addition of a broad [C II]$_{158\ \mu m}$ component to the spectral fit is not preferred by the NOEMA data (see Appendix D). We have checked that the continuum fluxes in the lower- and higher-frequency sidebands are consistent within ∼2%. This ensures that the continuum of J1148+5251, determined from the full ∼7.6 GHz sideband, is consistent with that determined solely from the single ∼3.8 GHz baseband containing the [C II]$_{158\ \mu m}$ line. We also show in Appendix E that the choice of the line masking width and the flux calibration

Table 2
Atomic FSL Flux Measurements from the Line Maps
($\Delta v = 1.2 \times \mathrm{FWHM_{C\ II}} = 482$ km s^{-1}), Flux-corrected by 1/0.84

3″ Aperture	[N II]$_{205\ \mu m}$	[C II]$_{158\ \mu m}$	[O I]$_{146\ \mu m}$
S/N	3.7	42.0	5.4
$S_{\rm line}\Delta v$ [Jy km s^{-1}]	0.5 ± 0.3	10.2 ± 0.5	1.0 ± 0.6
$L_{\rm line}$ [$10^9 L_\odot$]	0.4 ± 0.2	10.6 ± 0.5	1.1 ± 0.7
$L'_{\rm line}$[10^9 K km s^{-1} pc^{-2}]	4.4 ± 2.1	48.1 ± 2.5	4.1 ± 2.4
Peak [C II] pixel	[N II]$_{205\ \mu m}$	[C II]$_{158\ \mu m}$	[O I]$_{146\ \mu m}$
S/N	1.1	42.0	5.4
$S_{\rm line}\Delta v$ [Jy km s^{-1}]	<0.12	6.4 ± 0.2	1.0 ± 0.2
$L_{\rm line}$ [$10^9 L_\odot$]	<0.10	6.7 ± 0.2	1.2 ± 0.2
$L'_{\rm line}$[10^9 K km s^{-1} pc^{-2}]	<1.0	30.4 ± 0.7	4.1 ± 0.8

Note. Upper limits are given at the 3σ level. The first three lines give the luminosity for the total integrated flux and the last three for the peak [C II]$_{158\ \mu m}$ surface brightness. All of the integrated fluxes are derived by applying residual scaling correction, and the luminosities are computed following the definitions of Solomon et al. (1997).

differences between the two ∼3.8 GHz basebands do not impact the recovered [C II]$_{158\ \mu m}$ line.

The presence of a broad [C II]$_{158\ \mu m}$ wing reported in previous works (Maiolino et al. 2012; Cicone et al. 2015) and its absence in the NOEMA data seems puzzling at first. Indeed, Cicone et al. (2015) reach a sensitivity in the [C II]$_{158\ \mu m}$ line comparable to ours (0.46 mJy beam^{-1} versus 0.45 mJy beam^{-1} per 100 km s^{-1} channel) and have a similar angular resolution ($1\farcs3 \times 1\farcs2$ versus $1\farcs97 \times 1\farcs59$). However, their observations were performed with a smaller number of antennas (six, corresponding to 15 baselines, whereas the new observations were done with eight to nine, corresponding to 28–36 baselines), using a correlator that provided a spectral coverage (∼3.6 GHz) twice as narrow as that of the new observations (∼7.7 GHz) around the [C II]$_{158\ \mu m}$ line. Hence, the discrepancy cannot stem from sensitivity or resolution issues, and we expect that, due to our slightly larger beam, larger number of antennas, and higher imaging fidelity, we would be more sensitive, if anything, to extended [C II]$_{158\ \mu m}$ structures in J1148+5251 compared to earlier data. The wider spectral coverage of the new *Polyfix* also enables us to better constrain the dust continuum emission and the exact shape of a potential broad [C II]$_{158\ \mu m}$ emission line.

In Appendix F, we discuss in detail the origins of these discrepancies, which can be ascribed to a combination of (i) continuum subtraction and (ii) residual scaling effects. We show that when taking these into account, the previous PdBI and new NOEMA data are consistent. We present the combined data in Appendix F, and find that, using the same approach as used here, broad [C II]$_{158\ \mu m}$ line wings are only tentatively recovered in the merged PdBI and NOEMA data set. We finally note that the statistical methodology used here to assess the presence of an outflow is arguably quite conservative. Indeed, with the sensitivity and spectral coverage of the data at hand, only extremely powerful outflows would produce a broad line component whose significance is such that a ξ^2 or BIC criterion would prefer a double-component fit over a single-component one. In low-redshift studies, it is common to use multiple diagnostics (PV diagrams and other outflow tracers) to assume the presence of an outflow first, and then fit the spectral profile with two components (see, e.g., the discussion in Cicone et al. 2014). In any case, these

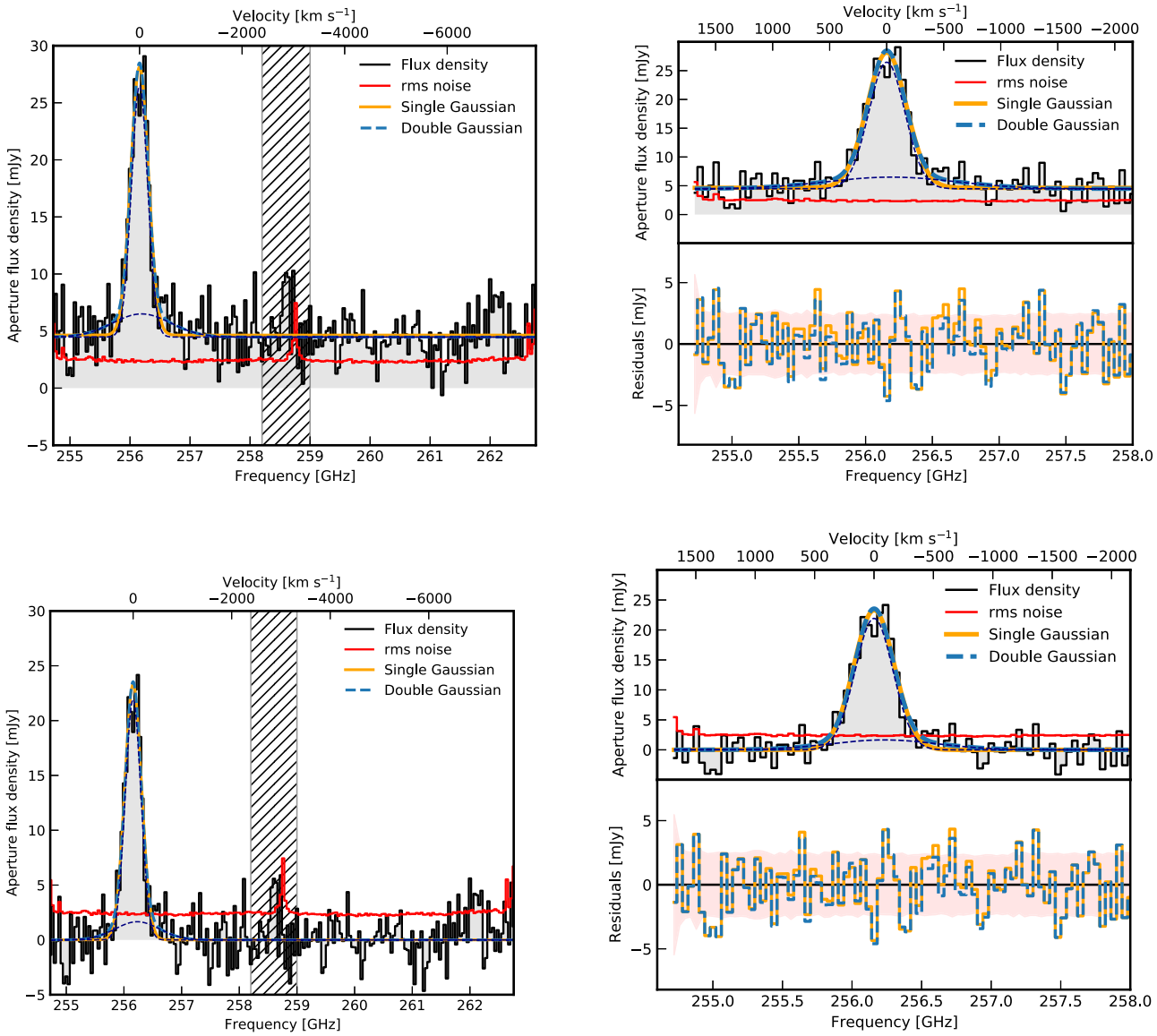


Figure 5. The total (top panels) and continuum-subtracted (bottom panels) spectra of the [C II]$_{158\ \mu m}$ line (black), extracted in a $r = 3''$ aperture using residual scaling and one- and two-component Gaussian fits (the orange line and the dashed–dotted blue line, respectively). The thin dashed dark blue lines show the two components of the double-Gaussian model. Both models are fitted to the entire frequency range, with the exception of the overlap between the two sidebands that is coincident with an atmospheric absorption feature (hatched in gray) and the 262 GHz feature (see the text). The right panels show a zoomed-in version of the left plots and the residuals of the two models. The shaded red areas in the bottom of the right panels show the 1σ noise level, computed using the rms noise in each channel in mJy beam^{-1} with the sigma-clipping scaled accordingly for the number of beams in the $r = 3''$ aperture. The median noise level at $\nu_{obs} > 263$ GHz is 2.36 ± 0.14 mJy, whereas a direct rms estimate from the continuum-subtracted spectrum at the same frequencies gives 2.00 ± 0.15 mJy. We find no evidence for a broad [C II]$_{158\ \mu m}$ emission line in the new NOEMA data (see the text for details).

new NOEMA data, thanks to the improved continuum subtraction and analysis methodology, indicate a much less prominent broad component than previously reported, and so rule out the presence of an extremely strong high-velocity outflow. We have, however, provided the two-Gaussian best-fit results above, in case future observations provide ancillary evidence in favor of an outflow.

4.2. Spatially Extended [C II]$_{158\ \mu m}$ Emission

The [C II]$_{158\ \mu m}$ emission is spatially extended (Figure 3). In Figure 6, we show the dust and [C II]$_{158\ \mu m}$ radial profiles to investigate their spatial extension. The dust continuum emission (at ∼259 GHz) is as extended (within 1σ errors) as the [C II]$_{158\ \mu m}$ emission (up to $\theta = 2.51^{+0.46}_{-0.25}$ arcsec, at the 3σ level; see Figure 6, leftmost panel), suggesting that both trace star-forming material with physical conditions similar to those that we normally ascribe to the ISM of galaxies, rather than an extended [C II]$_{158\ \mu m}$ halo[14] or outflow. This corresponds to a radius of $r = 9.8^{+3.3}_{-2.1}$kpc, accounting for beam convolution. This is at least twice as large as any of the 27 quasars observed in [C II]$_{158\ \mu m}$ by Venemans et al. (2020), confirming earlier reports (Maiolino et al. 2012; Cicone et al. 2015) that J1148+5251 is an outlier in terms of [C II]$_{158\ \mu m}$ emission extension. This result holds as well if the dust extension is measured from other spectral setups (e.g., Figure 1).

[14] We consider here and hereafter a [C II]$_{158\ \mu m}$ halo to be significant emission beyond that of the dust continuum emission (e.g., Fujimoto et al. 2019, 2020; Herrera-Camus et al. 2021).

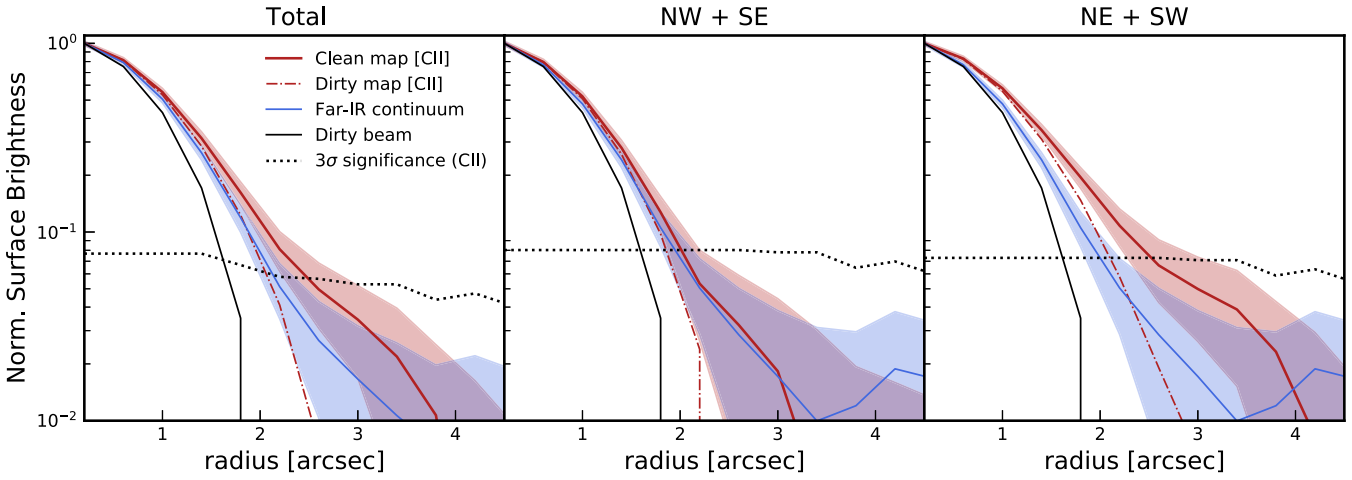


Figure 6. [C II]$_{158\ \mu m}$ (red) and dust continuum emission (blue) profiles for J1148+5251, which both extend up to $\theta = 2.51^{+0.46}_{-0.25}$ arcsec at the 3σ level, corresponding to $r = 9.8^{+3.3}_{-2.1}$ (accounting for beam convolution). The shaded areas show the corresponding 1σ noise level. A point-source profile is shown in black and the dirty (before cleaning and residual scaling) profile is shown in dashed–dotted red. The three panels show, from left to right: the radial profile integrated over the full 2π, only in the NW and SE quadrants, and finally only in the NE and SE quadrants (e.g., along the extended emission seen in Figure 3). In the latter case, the [C II]$_{158\ \mu m}$ emission is more extended than the FIR continuum (5.8σ significance).

The extension of [C II]$_{158\ \mu m}$ is asymmetric, however, with a prominent NE–SW axis (Figure 3, although this is less pronounced with a larger channel width; see Figure 8, first panel). In the second and third panels of Figure 6, we compare the dust continuum and the [C II]$_{158\ \mu m}$ radial surface brightness profile for the radially averaged case, the NE–SW axis, and the NW–SE axis (see Figure 3). While we find no evidence for an extended [C II]$_{158\ \mu m}$ halo when averaging radially (or along the NW–SE axis), along the NE–SW axis the [C II]$_{158\ \mu m}$ emission is significantly more extended than the dust continuum (5.8σ).

We finally explore the extension of the [C II]$_{158\ \mu m}$ emission and the dust continuum directly in the *uv* plane. To that end, we use the UV_FIT and UV_CIRCLE routines in GILDAS/MAPPING to fit the visibilities with a point source and 2D Gaussian emission model, and then bin the modeled and observed visibilities radially. We plot the real part of the visibilities against the *uv* radius in Figure 7. In such plots, a point source gives a constant flux density at all *uv* radii, while a Gaussian emission model yields a Gaussian profile centered at $r = 0$. We find good agreement between the observed visibilities and a composite emission model comprising a point source and a 2D Gaussian. We fit both a circular Gaussian and an elliptical Gaussian to the dust and [C II]$_{158\ \mu m}$ continuum visibilities. For the [C II]$_{158\ \mu m}$ emission, the best-fit model gives a corrected velocity-integrated flux of 4.2 ± 0.5 Jy km s^{-1} in the point-source component, and 5.0 ± 0.5 Jy km s^{-1} in the extended Gaussian, in good agreement with the flux derived from the line map (Table 2) and the fitted spectrum (see Appendix D). The elliptical Gaussian models yield velocity-integrated fluxes of 5.0 ± 0.3 Jy km s^{-1} and 5.5 ± 0.4 Jy km s^{-1} for the point-source and resolved components, respectively. In either case, we are consistent with the large fraction of emission coming from the unresolved component reported in Cicone et al. (2015), but not with the overall flux, which is possibly due to continuum subtraction differences, as discussed in Appendix F. Additionally, the unresolved flux is consistent with that measured at higher resolution (Walter et al. 2009a), suggesting the difference in total flux is due to the extended component being resolved out in high-resolution configurations.

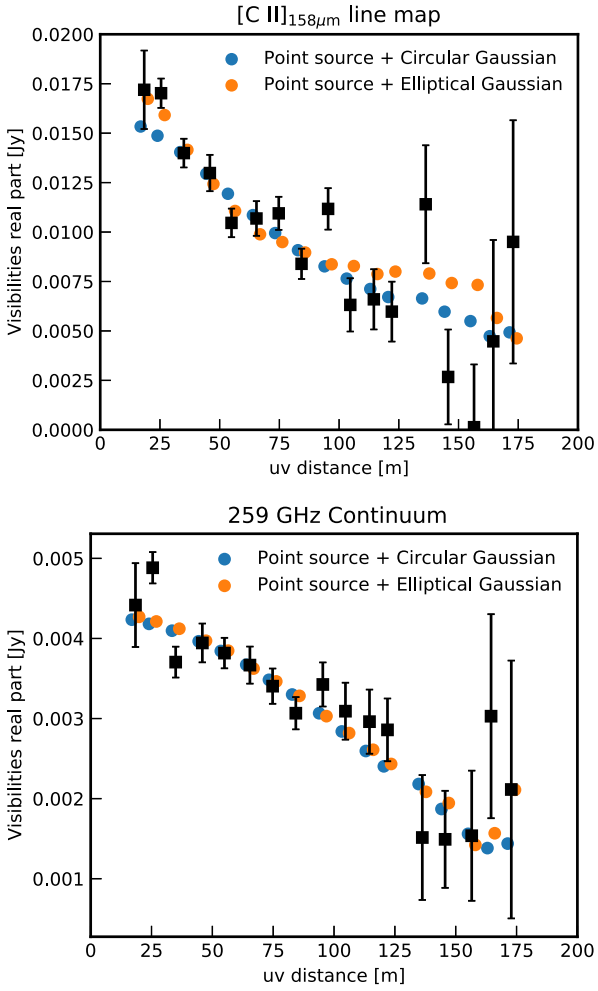


Figure 7. Observed (black) and modeled (blue and orange) real parts of the visibilities for the [C II]$_{158\ \mu m}$ emission (integrated over $\Delta v = 482$km s^{-1}) and dust continuum in J1148+5251. The model points are slightly offset for presentation purposes. The difference between the two models (blue: point source + circular Gaussian; orange: point source + elliptical Gaussian) is not statistically significant (p-value = 0.83; e.g., 0.96σ significance).

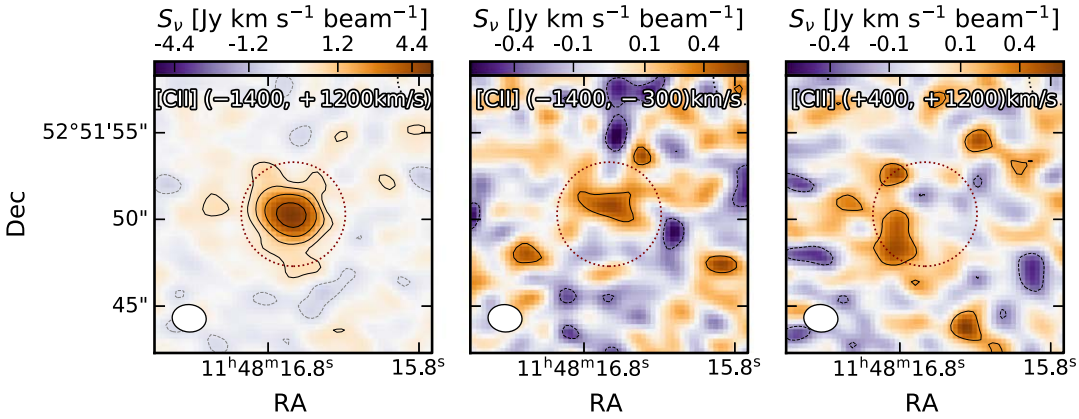


Figure 8. From left to right: a map of the [C II]$_{158\ \mu m}$ emission, averaged over the velocity ranges (−1400, 1200) km s^{-1}, (−1400, 300) km s^{-1}, and (+400, +1200) km s^{-1}. These velocity ranges are similar to those presented in Cicone et al. (2015), who reported 6σ [C II]$_{158\ \mu m}$ clumps at 2″–4″ from the source center in the blue-/redshifted wings of the [C II]$_{158\ \mu m}$ emission. Such spatially and spectrally offset emission is not recovered in the NOEMA data. The 1σ rms values in the above three maps are 0.27, 0.14, and 0.15 mJy beam^{-1}. This figure shows contours in logarithmic increments (−4, −2, 2, 4, 8, 16, 32)σ (rms).

The FWHM of the [C II]$_{158\ \mu m}$ Gaussian component is FWHM = 1.″6 ± 0.″2(9 ± 1 kpc), or minor/major axes $a = 3.''6 \pm 0.''3$ (20 ± 2 kpc) and $b = 1.''8 \pm 0.''2$ (10 ± 1 kpc) for the elliptical model. This is in agreement with the scale of the 3σ extension directly measured on the cleaned image. The elliptical Gaussian has a major/minor axis difference and angle (PA = 53 ± 4 deg) in agreement with the asymmetric [C II]$_{158\ \mu m}$ emission discussed above. However, a likelihood ratio test does not prefer the elliptical Gaussian model over the circular one (p-value = 0.83; e.g., 0.96σ significance). We do not find any difference between the elliptical Gaussian and circular Gaussian models for the dust emission (see Figure 7). The best-fit model for the dust emission gives a flux density of 1.0 ± 0.7 mJy and 3.3 ± 0.7 mJy for the unresolved/resolved components, respectively, with the sum in agreement with the measurement of the aperture-integrated flux density (Table 1). The dust uv profile (Figure 7, bottom panel) does not show clear evidence of a flattening at large uv distances that is characteristic of a point source. The Gaussian component has an FWHM of $r = 0.''7 \pm 0.''1$ (3.9 ± 0.6 kpc).

Cicone et al. (2015) reported a complex velocity structure of the [C II]$_{158\ \mu m}$ outflow, with emission clumps detected up to $r \sim 30$ kpc and ~ 1000 km s^{-1} offsets from the central emission, particularly visible in an emission line map integrated over a (−1400, 1200) km s^{-1} interval (we show in Appendix F how we recover these structures in the previous PdBI data, although at a lower significance level). Such features are not recovered in the new NOEMA data when averaging over a similar velocity interval (Figure 8, left panel; see also Appendix F). The [C II]$_{158\ \mu m}$ emission is mostly concentrated within 3″ (∼11 kpc), and no significant emission is recovered beyond that radius.[15] We further show in Appendix G that no significant velocity structure is detected in J1148+5251 in the NOEMA data, neither by inspecting the channel maps (with channel width $\Delta v = 120$ km s^{-1}) nor by means of a kinematical analysis.

[15] Following the analysis of Cicone et al. (2015), we also plot the blue- and redshifted components ((−1400, −300) km s^{-1} and (+400, +1200) km s^{-1}) of the [C II]$_{158\ \mu m}$ emission, and find only marginal detections (3.0 and 3.4σ) that are not spatially offset (Figure 8).

5. ISM Properties

5.1. [C II]$_{158\ \mu m}$ Emission

In the following analysis, we adopt luminosities measured from the line maps. We measure a [C II]$_{158\ \mu m}$ line luminosity $L_{[\rm C\ II]} = (10.6 \pm 0.5) \times 10^8 L_\odot$ ($L'_{[\rm C\ II]} = (48.1 \pm 2.5) \times 10^9$ K km s^{-1}pc^{-2}). Following the [C II]–SFR relation of De Looze et al. (2014) for high-redshift ($z > 0.5$) galaxies, we find SFR = 2041 ± 111 $M_\odot$ yr^{-1}, in good agreement with the SFR inferred from the continuum luminosities. Using the De Looze et al. (2014) calibration for AGNs does lower the result (SFR = 857 ± 35 $M_\odot$ yr^{-1}), and that for ULIRGS increases the inferred SFR (SFR = 5562 ± 257 $M_\odot$ yr^{-1}). This agreement between the [C II]$_{158\ \mu m}$ and the infrared luminosity-based SFR is also observed in other high-redshift quasars (e.g., Novak et al. 2019; Venemans et al. 2020) where the FIR luminosity is smaller. We caution that the SFR–[C II]$_{158\ \mu m}$ relations used above are dependent on the FIR luminosity and the FIR surface brightness of the galaxy populations used to calibrate them (e.g., Díaz-Santos et al. 2017; Herrera-Camus et al. 2018b). These SFR values should only be used to compare with other high-redshift sources where the FIR is not well constrained. For J1148+5251, the [C II]/FIR ratio is $\simeq (7.8 \pm 1.3) \times 10^{-4}$. We thus use the appropriate "high $\Sigma_{\rm FIR}$" [C II]$_{158\ \mu m}$–SFR calibration from Herrera-Camus et al. (2018b) and find SFR = 3100 ±1600 $M_\odot$ yr^{-1}, in agreement with the other estimates presented above.

Following Weiß et al. (2003, 2005), in the optically thin limit, the total mass of ions X emitting photons with rest-frame frequency ν_{ij} stemming from a transition between the i and j levels can be derived from the observed luminosity as:

$$M_X = m_X \frac{8\pi k \nu_{ij}^2}{hc^3 A_{ij}} Q(T_{\rm ex}) \frac{1}{g_i} e^{-T_{\rm ex}/T_i} L'_{[X_{i\rightarrow j}]}, \quad (1)$$

where k is the Boltzmann constant, c is the speed of light, h is the Plank constant, m_X is the mass of a single ion X, $Q(T_{\rm ex}) = \sum_i g_i e^{-T_i/T_{\rm ex}}$ is the partition function of the species, with g_i being the statistical weight of level i, T_i being the energy of (above-ground) level i, $T_{\rm ex}$ being the excitation temperature of the $i \rightarrow j$ transition, and $L'_{[X_{ij}]}$ being the observed integrated source brightness temperature of the line in K km s^{-1} pc^{-2}. Note

that Equation (1) neglects heating from the CMB, which is negligible for the [O I]$_{146\,\mu m}$, [C II]$_{158\,\mu m}$, and [N II]$_{205\,\mu m}$ transitions, but not [C I]$_{369\,\mu m}$ at $z \sim 6.4$. For C^+, Equation (1) reduces to:

$$M_{C^+}/M_\odot = 2.92 \times 10^{-4} Q(T_{ex}) \frac{1}{4} e^{-91.2/T_{ex}} L'_{[C\,II]}, \quad (2)$$

where $Q(T_{ex}) = 2 + 4e^{91.2/T_{ex}}$ is the [C II]$_{158\,\mu m}$ partition function. The optically thin limit assumption, while widespread in the literature, is uncertain at higher redshift, since optical depth measurements, although pointing to moderate values, are scarce (e.g., Neri et al. 2014; Gullberg et al. 2015). Lagache et al. (2018) and Vallini et al. (2015) note that in the optically thick limit, only emission from PDRs would reach the observer. As we will show in Section 5.4, most of the [C II]$_{158\,\mu m}$ emission in J1148+5251 indeed comes from PDRs, and hence we do not expect the optically thin limit assumption to affect our results. Assuming an excitation temperature $T_{ex} = 50$ K (from the CO modeling; Riechers et al. 2009), we find $M_{C^+} = (5.8 \pm 0.3) \times 10^7 M_\odot$. This is five times the neutral carbon mass ($M_C = 1.1 \times 10^7 M_\odot$) measured by Riechers et al. (2009).

5.2. [N II]$_{205\,\mu m}$ Emission

We report an [N II]$_{205\,\mu m}$ marginal detection in J1148+5251 at S/N = 3.7 and an integrated ($r = 3''$) luminosity $L_{[N\,II]} = (0.4 \pm 0.2) \times 10^9 L_\odot$. This is in slight tension with the 3σ limit ($< 0.4 \times 10^9 L_\odot$) reported by Walter et al. (2009b) using the IRAM 30 m telescope. Nonetheless, we would expect better image fidelity with the new NOEMA facility. We consider the [N II]$_{205\,\mu m}$ detection marginal (3.7σ), and urge caution in interpretations that rely upon it.

The marginal ($1\farcs59/8.9$ kpc ~ 1 beam) offset between [N II]$_{205\,\mu m}$ and [C II]$_{158\,\mu m}$ in J1148+5251 could be of interest. On the one hand, spatial offsets between low- and high-ionization lines have been reported in other high-redshift quasars, most often between [C II]$_{158\,\mu m}$ and [O III]$_{88\,\mu m}$ (e.g., Novak et al. 2019). Spatial offsets have also been predicted in theoretical simulations (Katz et al. 2017, 2019), where they arise from different gas phases with different temperatures and densities. Although nitrogen and carbon have a similar ionization level, Katz et al. (2019) show that the [N II]$_{205\,\mu m}$ and [C II]$_{158\,\mu m}$ can arise from different gas phases, with [C II]$_{158\,\mu m}$ originating in lower-temperature and higher-density regions,[16] which could explain the offset of [N II]$_{205\,\mu m}$ toward the outskirts of J1148+5251. On the other hand, offsets often seen at low resolution in high-redshift galaxies can disappear in higher-resolution data once fainter emission components are detected (see,, e.g., HZ10 in Pavesi et al. 2016, 2019). Following Ferkinhoff et al. (2010, 2011), we derive the minimum H^+ for the [N II]$_{205\,\mu m}$ luminosity observed. To do so, we assume high densities and a high temperature (as found around O and B stars), such that all nitrogen in the H II regions is ionized. We use Equation (1) to derive the mass of N^+ in J1148+5251 from the observed luminosity, with $A_{10} = 2.1 \times 10^{-6}$ being the Einstein coefficient of the $^3P_1 \rightarrow {}^3P_0$ transition, $g_1 = 3$ being the statistical weight of the $^3P_1$ emitting level, $\nu_{10} = 1461.1$ GHz being the rest-frame frequency, and $g_t \simeq 9$ being the partition function. We can then derive the minimum H^+ mass by assuming the upper limit on the ionized nitrogen to ionized hydrogen ratio (i.e., $\chi(N^+) = N^+/H^+$) to be the total nitrogen abundance ratio $\chi(N)$, such that

$$M(H^+) \geqslant M_{N^+} \frac{m_N}{m_H \chi(N^+)} = \frac{L_{[N\,II]205\,\mu m}}{\frac{g_1}{g_t} A_{10} h \nu_{10}} \frac{m_H}{\chi(N^+)}. \quad (3)$$

We adopt the abundance value for H II regions $\xi(N) = 9.3 \times 10^{-5}$ from Savage & Sembach (1996). Hence, we estimate an ionized hydrogen mass $M(H^+) \geqslant (2.1 \pm 1.0) \times 10^9 M_\odot$ (2σ level). Using the H_2 gas mass from the CO luminosity (Riechers et al. 2009), the ionized to molecular gas ratio is $M(H^+)/M(H_2) > 0.1$. This is significantly higher than what is found by Ferkinhoff et al. 2011 (based on the compilation by Brauher et al. 2008) for local galaxies using the [N II] 122 μm line (<0.01). We caution here again that the [N II]$_{205\,\mu m}$ line is marginal.

The [C II]/FIR ratio ($\simeq (7.8 \pm 1.3) \times 10^{-4}$), [N II]/FIR ratio ($\sim (2.9 \pm 1.5) \times 10^{-5}$), and dust temperature (53 ± 8 K) are all in agreement with the ratio trends (extrapolated to the high temperature observed in J1148+5251) observed in local ULIRGS (Díaz-Santos et al. 2017) and high-redshift galaxies or quasars (De Breuck et al. 2019; Novak et al. 2019; Pavesi et al. 2019; Li et al. 2020; Pensabene et al. 2021; see Figure 9). We note that the [C II]/[N II] luminosity ratio (10.6 ± 3.7) is slightly low for the dense PDRs/X-ray-dominated regions (XDRs) expected around high-redshift quasars (e.g., Decarli et al. 2014; Pavesi et al. 2019), though the uncertainties are large given the marginal detection in the [N II]$_{205\,\mu m}$ line. Finally, we also test the Zhao et al. (2016), [N II]$_{205\,\mu m}$–SFR scaling relation derived from local ULIRGS, which gives SFR $= 794 \pm 274\,M_\odot\,yr^{-1}$, lower than the [C II]$_{158\,\mu m}$ and FIR-derived values. We note, however, that [N II]$_{205\,\mu m}$ is a poor tracer of the SFR in intense star-forming regions, such as J1148+5251, due to its low critical density (e.g., Herrera-Camus et al. 2016; Zhao et al. 2016).

5.3. [O I]$_{146\,\mu m}$ Emission

The peak of the [O I]$_{146\,\mu m}$ emission is located at the same position as the [C II]$_{158\,\mu m}$ emission. The [O I]$_{146\,\mu m}$/FIR ratio is 1.3×10^{-5}, in good agreement with that of local ULIRGS with comparable FIR surface flux density (Herrera-Camus et al. 2018a). The [O I]$_{146\,\mu m}$/[C II]$_{158\,\mu m}$ line luminosity ratio $L_{[O\,I]}/L_{[C\,II]} = 0.10 \pm 0.07$ is typical of that observed in high-redshift submillimeter galaxies and quasars (e.g., De Breuck et al. 2019; Yang et al. 2019; Li et al. 2020; Lee et al. 2021), and is at the higher end of the range spanned by local AGNs (e.g., Fernández-Ontiveros et al. 2016).

Again using Equation (1) for the [O I]$_{146\,\mu m}$ $^3P_0 \rightarrow {}^3P_1$ transition ($T_0 = 329$ K, $g_0 = 1$, $Q(T_{ex}) = 5 + 3e^{-329/T_{ex}} + e^{-228/T_{ex}}$), we derive a neutral oxygen mass

$$M_O/M_\odot = 6.19 \times 10^{-5} Q(T_{ex}) e^{329/T_{ex}} L'_{[O\,I]}. \quad (4)$$

Assuming an excitation temperature $T_{ex} = 50$ K (from the CO modeling; Riechers et al. 2009), we find $M_O = (9 \pm 5) \times 10^8 M_\odot$. This estimate is extremely sensitive to the excitation temperature, e.g., ranging from $0.7 \times 10^7 M_\odot$ at 200 K to $8 \times 10^8 M_\odot$ at $T_{ex} = 50$ K. Note that the above expression only applies in the optically thin limit, which is probably not the case for [O I]$_{146\,\mu m}$, therefore it underestimates the neutral oxygen mass.

[16] Although a minor fraction of [C II]$_{158\,\mu m}$ traces the same H II regions as [N II]$_{205\,\mu m}$; see Section 5.4.

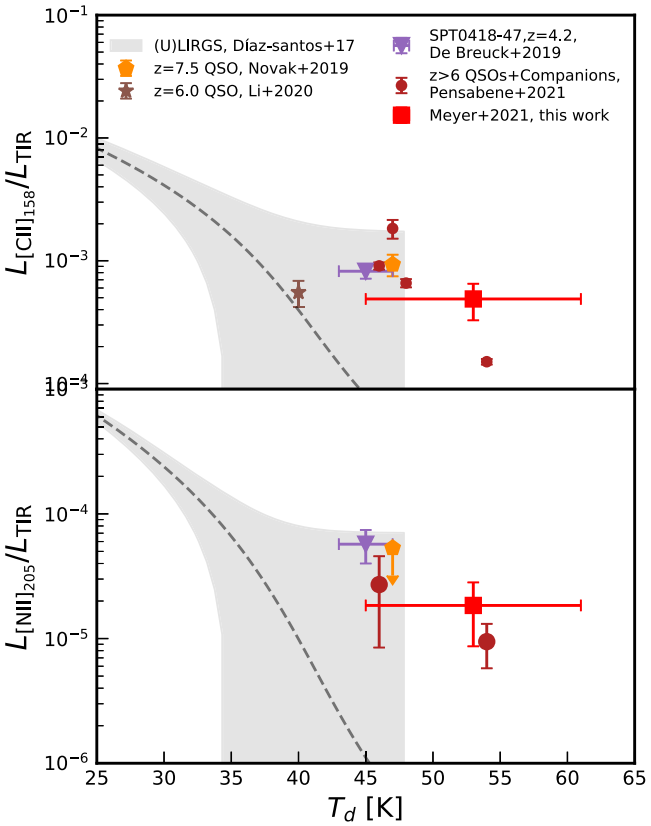


Figure 9. [C II]$_{158\ \mu m}$ and [N II]$_{205\ \mu m}$ line deficits of local (U)LIRGS (shaded gray; Díaz-Santos et al. 2017), the high-redshift galaxy SPT0418-47 (the purple triangle; De Breuck et al. 2019), and high-redshift quasars (the orange pentagon, dark orange star, and dark red circles; Novak et al. 2019; Li et al. 2020; Pensabene et al. 2021, respectively) and companion galaxies (the dark red circles; Pensabene et al. 2021). Our measurements for J1148+5251 are shown via the red squares.

5.4. CLOUDY Modeling of the FSL Ratios

We now use the FSL ratios to determine the physical properties of the ISM of J1148+5251. In order to do so, we make use of CLOUDY (Ferland et al. 2017), a spectral synthesis code designed to simulate the spectra of astrophysical plasmas used to study both low- and high-redshift galaxies' submillimeter lines. The grid of models used in this work was generated for studying both high-redshift quasar hosts and their companions, by Pensabene et al. (2021), to which we refer for further details. To summarize briefly, the model grid includes both PDR and XDR predictions for total hydrogen column densities $N_H/[cm^{-2}] = 10^{23}$–10^{24}, total hydrogen number density $1 < \log n/[cm^{-3}] < 6$, and local far-UV radiation field $2 < \log G/[G_0] < 6$ in units of Habing flux (for the PDRs) or X-ray flux $-2 < \log F_X/[erg\ s^{-1}\ cm^{-2} < 2] < 2$ (for the XDRs). For each combination of parameters, the fluxes of the various lines of interest are predicted, and the ISM conditions can be determined by comparing the observed line ratios.

Whereas [C II]$_{158\ \mu m}$ can originate from both the neutral and ionized gas phase, [O I]$_{146\ \mu m}$ and [C I]$_{369\ \mu m}$ originate solely in the neutral gas phase/PDRs. It is therefore crucial to determine which fraction of the [C II]$_{158\ \mu m}$ emission in J1148+5251 comes from the neutral gas. [N II]$_{205\ \mu m}$ and [C II]$_{158\ \mu m}$ have very close critical densities in ionized media, therefore the [C II]$_{158\ \mu m}$ to [N II]$_{205\ \mu m}$ ratio is primarily a function of the N^+/C^+ abundance ratio (e.g., Oberst et al. 2006). Photoionization models (e.g., Oberst et al. 2006; Pavesi et al. 2016; Croxall et al. 2017) predict a relatively constant ratio $(2.5 - 3)$ for [N II]$_{205\ \mu m}$/[C II]$^{ion}_{158\mu m}$ for a large range of electron densities. For consistency with the existing literature, we adopt [N II]$_{205\ \mu m}$/[C II]$^{ion}_{158\mu m} = 3$. Any deviation from that ratio can be interpreted as [C II]$_{158\ \mu m}$ emission from the neutral phase. The fraction of [C II]$_{158\ \mu m}$ emission originating in the neutral phase is therefore

$$f([\mathrm{C\ II}], \mathrm{neutral}) \simeq 1 - 3\frac{L_{[\mathrm{N\ II}]_{205\ \mu m}}}{L_{[\mathrm{CII}]_{158\ \mu m}}}. \quad (5)$$

The ratio of the luminosities measured in this work for J1148+5251 is 27 ± 13 for the aperture-integrated ($r = 3''$) flux and >100 (2σ level) at the peak of the [C II]$_{158\ \mu m}$ emission. In either case, most of the [C II]$_{158\ \mu m}$ emission (88%–97%) comes from the neutral phase.

Given the resolution of the NOEMA data, we use the $r = 3''$ aperture-integrated line luminosities to compute line luminosity ratios and compare them to the grid of CLOUDY models. In order to properly include the [C I]$_{369\ \mu m}$ measurements from Riechers et al. (2009), we have repeated the line map procedure detailed in Section 2 on the original [C I]$_{369\ \mu m}$ data. We produce a line map with width $\Delta v = 482$ km s^{-1}, and integrate the flux up to $r = 3''$, finding $S_{[C\ I]\ 369\ \mu m}\Delta v = 0.45 \pm 0.16$ Jy km s^{-1} and a line luminosity $L_{[C\ I]\ 369\ \mu m} = (0.20 \pm 0.07) \times 10^9 L_\odot$. The new luminosity value is in agreement, within 1.4σ, with the previously published value of $(0.10 \pm 0.02) \times 10^9 L_\odot$ (Riechers et al. 2009). The difference between the two measurements can be explained by the larger aperture, and is comparable to that seen for [C II]$_{158\ \mu m}$ (see Appendix A).

We show the radiation field and density predictions of CLOUDY for the observed FSL ratios in Figures 10 and 11. We find that the different line ratios are not perfectly reproduced for a single density and radiation field by the chosen grid of models. However, the [C II]$^{neutral}_{158\ \mu m}$/[C I]$_{369\ \mu m}$ luminosity ratio (47 ± 3) excludes XDR models, which cannot reproduce such high ratios (the maximum possible being $\sim$15; Figure 10; e.g., Venemans et al. 2017a, 2017b; Novak et al. 2019; Pensabene et al. 2021). Besides, our XDR model grid cannot reproduce all of the FSL to FIR luminosity ratios with a single hydrogen number density and X-ray flux. We note that this result, based on the analysis of the FSLs, is in tension with Gallerani et al. (2014), who concluded that an XDR component is needed in J1148+5251 to explain their reported CO(17–16) line. However, as noted by the authors, this line is potentially contaminated by a nearby OH^+ emission line, and thus additional observations of high-J CO lines are needed to clarify the situation.

The PDR models in agreement with the observed ratios (except [O I]$_{146\ \mu m}$/[C I]$_{369\ \mu m}$) have an H I column density of $N_{H\ I} = 10^{23}$ cm^{-2}, high radiation fields ($10^{3.5-4.5}\ G_0$), and moderate hydrogen number densities ($n \simeq 10^{3.5-4.5}$ cm^{-3}), commensurable with other studies of high-redshift quasars (e.g., Novak et al. 2019; Pensabene et al. 2021). The model grids do not reproduce the observed [N II]$_{205\ \mu m}$/[C II]$_{158\ \mu m}$ ratio, since it was not created to model the ionized phase (H II regions) traced by [N II]$_{205\ \mu m}$ emission. The [O I]$_{146\ \mu m}$/[C I]$_{369\ \mu m}$ discrepancy could stem from the different quality and resolution of the data, as well as the low S/N of both lines. Another possibility is that a fraction of the [C II]$_{158\ \mu m}$ emission could come from collisional excitation in the cold neutral medium, rather than solely from the PDRs, as is the case for [O I]$_{146\ \mu m}$ and [C I]$_{369\ \mu m}$, leading to a small discrepancy between the ratios

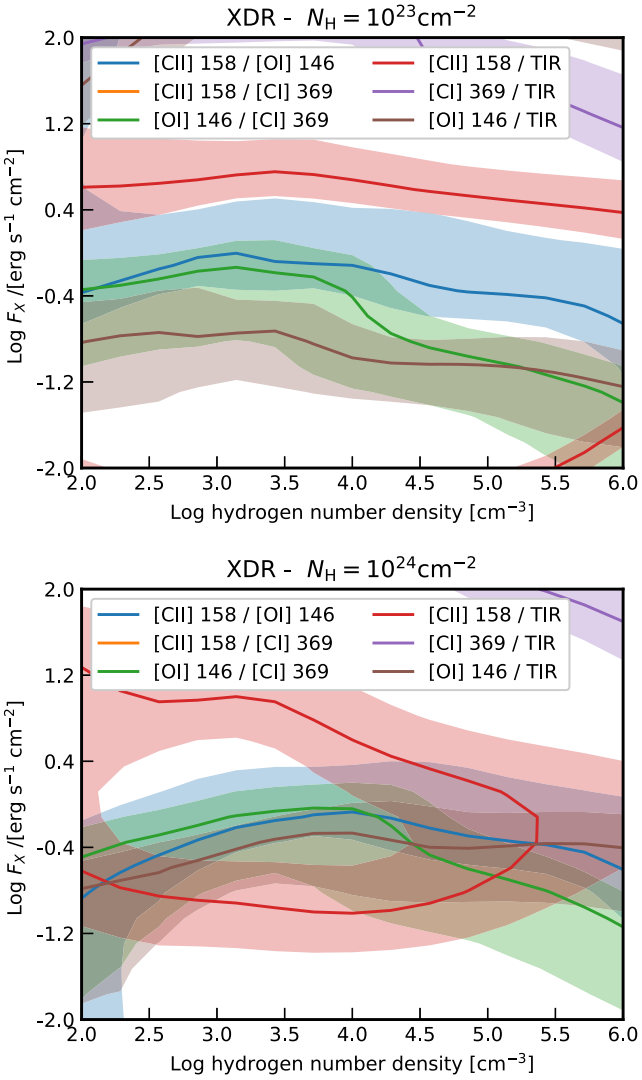


Figure 10. ISM constraints for J1148+5251 from the FSL ratios predicted by CLOUDY for XDRs with hydrogen column densities $N_H/[\mathrm{cm}^{-2}] = 10^{23}$ (top panel) and $N_H/[\mathrm{cm}^{-2}] = 10^{24}$ (lower panel). The observed ratio constraints from the aperture-integrated fluxes are plotted in solid lines, and the $\pm 1\sigma$ values in the shaded areas of the same color. The ratios absent from the plots (such as the [C II]$_{158\ \mu m}$ ratios) are not reproduced by the XDR grid of models.

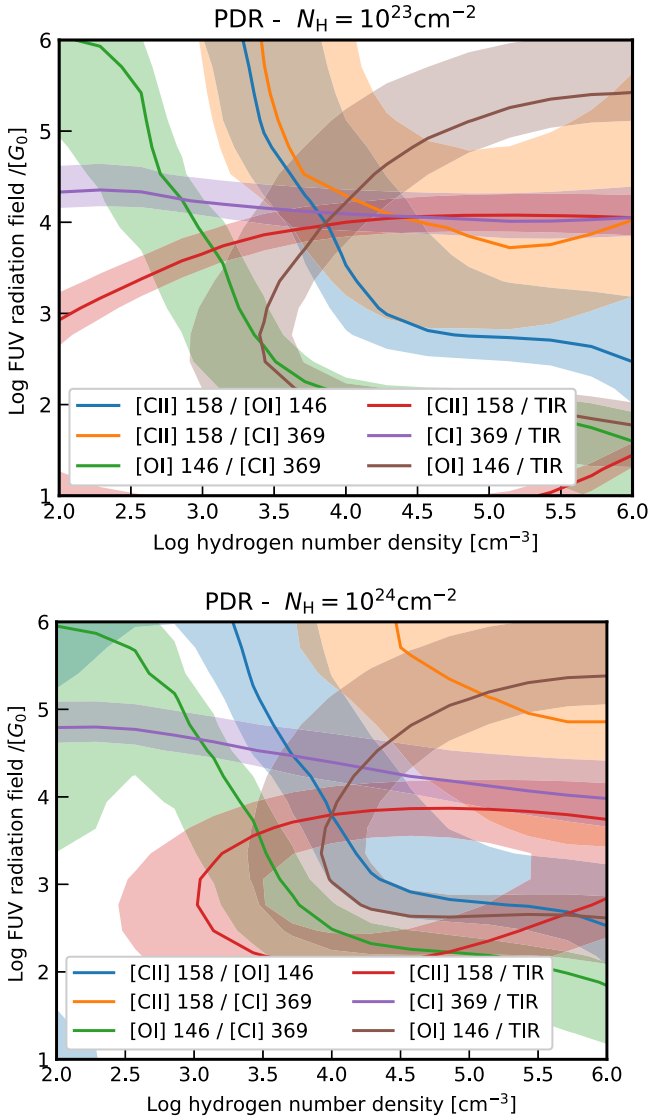


Figure 11. ISM constraints from the FSL ratios predicted by CLOUDY for PDRs with hydrogen column densities $N_H/[\mathrm{cm}^{-2}] = 10^{23}$ (top panel) and $N_H/[\mathrm{cm}^{-2}] = 10^{24}$ (lower panel). The observed ratio constraints from the aperture-integrated fluxes are plotted in solid lines, and the $\pm 1\sigma$ values in the shaded areas of the same color.

involving the [C II]$_{158\ \mu m}$line and others in our PDR-only models. This hypothesis is supported by the spatial extent of the [C II]$_{158\ \mu m}$ line emission (Section 4.2), which is beyond what is normally observed for the disk component of $z \sim 6$ massive star-forming galaxies and other quasar hosts (e.g., Venemans et al. 2020). Deeper and higher-resolution observations of the inner and outer [C II]$_{158\ \mu m}$-emitting regions, combining the presence or absence of [O I]$_{146\ \mu m}$, [N II]$_{205\ \mu m}$, and [C I]$_{369\ \mu m}$, would be required to further investigate the ISM of J1148+5251.

6. Conclusions

We report new NOEMA observations of the $z = 6.42$ quasar J1148+5251 in the atomic FSLs of [C II]$_{158\ \mu m}$, [O I]$_{146\ \mu m}$, and [N II]$_{205\ \mu m}$, and the underlying dust continuum emission. The high-fidelity data, together with the large instantaneous bandwidths that NOEMA provides, enabled us to revisit the properties of the quasar's host galaxy and derive the physical conditions of its ISM. The main conclusions of this paper are as follows:

1. A *uv* plane analysis confirms the presence of an extended [C II]$_{158\ \mu m}$ and dust emission component (FWHM = $1\farcs6 \pm 0\farcs2 (9 \pm 1$ kpc)), accounting for ~50%–60% of the total [C II]$_{158\ \mu m}$ and most of the dust emission, in agreement with earlier studies (Maiolino et al. 2012; Cicone et al. 2015). J1148+5251 thus remains an outlier with very extended [C II]$_{158\ \mu m}$ and dust emission compared to other $z > 6$ quasars (e.g., Venemans et al. 2020).
2. The [C II]$_{158\ \mu m}$ emission shows a similar spatial extent as the FIR dust when averaged radially (up to $\theta = 2.51^{+0.46}_{-0.25}$ arcsec, corresponding to $r = 9.8^{+3.3}_{-2.1}$ physical kpc, accounting for the beam convolution). However, if the [C II]$_{158\ \mu m}$ emission is examined only along its NE–SW axis, a significant (5.8σ) excess [C II]$_{158\ \mu m}$ emission (w.r.t. to the dust) is detected.

3. The $[\mathrm{C\,II}]_{158\,\mu\mathrm{m}}$ line profile can be fitted with a single Gaussian with a FWHM of $408 \pm 23\,\mathrm{km\,s^{-1}}$. The new NOEMA data has enabled us to reassess the significance of the broad $[\mathrm{C\,II}]_{158\,\mu\mathrm{m}}$ line wings reported in previous studies. We find that an additional broad $[\mathrm{C\,II}]_{158\,\mu\mathrm{m}}$ component is not statistically required to describe the NOEMA data (or the merged NOEMA and previous PdBI data).
4. We report the detection of $[\mathrm{O\,I}]_{146\,\mu\mathrm{m}}$ and $[\mathrm{N\,II}]_{205\,\mu\mathrm{m}}$ (tentatively) in J1148+5251. Using various empirical relations, we report a C^+ mass of $M_{C^+} = (2.7 \pm 0.1) \times 10^7 M_\odot$, an oxygen mass of $M_O = (12 \pm 4) \times 10^8 M_\odot$, and a lower limit on the ionized hydrogen mass $M_{H^+} > (4.6 \pm 0.16) \times 10^8 M_\odot (2\sigma$ level).
5. The FSL line ratios are consistent with the trends observed in local (U)LIRGs. We find that a large fraction ($\sim 90\%$) of the $[\mathrm{C\,II}]_{158\,\mu\mathrm{m}}$ emission originates in the neutral phase (PDR) of the gas.
6. We have compared CLOUDY models to the observed FSL ratios in J1148+5251. The $[\mathrm{C\,II}]_{158\,\mu\mathrm{m}}/[\mathrm{C\,I}]_{369\,\mu\mathrm{m}}$ ratio and the multiple FSL to FIR ratios exclude XDR models in favor of PDRs. We find good agreement for models that have a high radiation field ($10^{3.5-4.5}\,G_0$), moderate hydrogen number densities ($n \simeq 10^{3.5-4.5}\,\mathrm{cm^{-3}}$), and H I column density $N_{\mathrm{H\,I}} = 10^{23}\,\mathrm{cm^{-2}}$.

The results described here highlight the importance of large instantaneous bandwidths when observing high-redshift quasars (or galaxies) to search for weak extended emission of atomic or molecular lines. Our findings enabled a renewed view on the host galaxy of the J1148+5251 quasar, shedding light on the feedback activity and providing new constraints on the excitation conditions of its ISM that appear similar to what is found in local ULIRGs. Higher-angular-resolution and higher-sensitivity data, in particular for the $[\mathrm{C\,I}]_{369\,\mu\mathrm{m}}$ emission line, would be required to put additional constraints on the gas density and the ionization source of J1148+5251, and further explore its properties.

The authors thank the anonymous referee for useful suggestions that improved the manuscript. R.A.M., F.W., and M.N. acknowledge support from the ERC Advanced Grant 740246 (Cosmic_Gas). D.R. acknowledges support from the National Science Foundation under grant Nos. AST-1614213 and AST-1910107. D.R. also acknowledges support from the Alexander von Humboldt Foundation through a Humboldt Research Fellowship for Experienced Researchers.

This work is based on observations carried out with the IRAM NOrthern Extended Millimeter Array (NOEMA). IRAM is supported by INSU/CNRS (France), MPG (Germany), and IGN (Spain). The authors would like to wholeheartedly thank the staff at IRAM for their help with the reduction and analysis software GILDAS; and in particular M. Krips, V. de Souza, C. Herrera, and J.-M. Winters.

Facility: NOEMA (IRAM).

Software: astropy (The Astropy Collaboration et al. 2018), CLOUDY (Ferland et al. 2017), Numpy (Harris et al. 2020), Scipy (Virtanen et al. 2020), Matplotlib (Hunter 2007), Interferopy (Boogaard, Meyer & Novak 2021).

Appendix A
Curve of Growth Analysis

In this appendix, we investigate what is the size of aperture that is necessary to recover most of the continuum or $[\mathrm{C\,II}]_{158\,\mu\mathrm{m}}$ line fluxes. Figure 12 shows the line flux density of $[\mathrm{C\,II}]_{158\,\mu\mathrm{m}}$, $[\mathrm{O\,I}]_{146\,\mu\mathrm{m}}$, and $[\mathrm{N\,II}]_{205\,\mu\mathrm{m}}$, as well as the continuum flux density, as a function of increasing aperture radius. We find that all of the line/continuum fluxes reach a maximum or plateau at an aperture radius $r = 3''$, which corresponds to 16.9 kpc at $z = 6.42$. The $[\mathrm{C\,II}]_{158\,\mu\mathrm{m}}$ flux presents tentative evidence for additional flux up to $4''$ ($\sim 1\,\mathrm{Jy\,km\,s^{-1}}$), but this is within the 1σ errors. Note that at large radii, where there is no more cleaned flux, residual scaling can become numerically unstable. Throughout this paper, an aperture of $r = 3''$ is therefore adopted for measurements, unless specified otherwise.

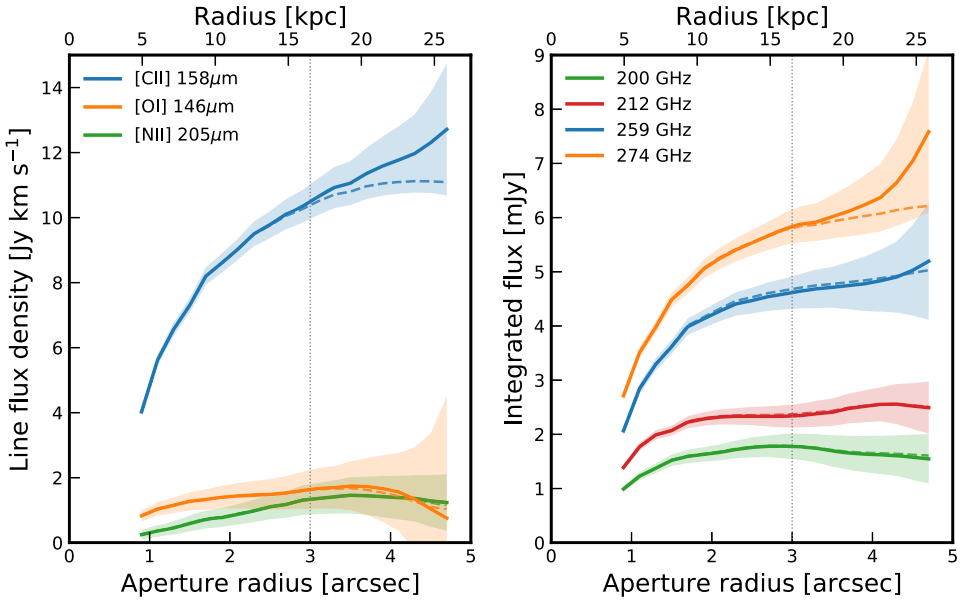


Figure 12. FSL flux densities (left panel) and integrated continuum flux (right panel) as a function of aperture radius. The solid and dashed lines show the fluxes with and without residual scaling correction (see Section 2), respectively. The final aperture radius of $3''$ was chosen to encompass all of the $[\mathrm{C\,II}]_{158\,\mu\mathrm{m}}$ emission and the continuum at the higher frequencies.

Appendix B
Multiscale and Högbom Cleaning Methods

In this appendix, we briefly detail our experiments with different cleaning methods for our interferometric data. Högbom cleaning (Högbom 1974) is one of the standard methods for cleaning interferometric data. It relies on iteratively finding peaks in the data, and subtracting the dirty beam at that location, until the residuals reach a desired level. It is particularly efficient for point sources, but struggles with large-scale emission, which it tries to reconstruct using a multitude of point sources. In that case, the so-called multiscale algorithms, which convolve the beam with various Gaussians to subtract larger scales, are preferable (e.g., Wakker & Schwarz 1988).

Figure 13 shows the clean map, the dirty map, and the residuals for the Högbom and multiscale clean on the [C II]$_{158\ \mu m}$ map (integrated over 482 km s^{-1}). Clearly, the Högbom clean residuals show a flat excess of 2σ flux filling the 3″ aperture, which would not be expected if the source was a single (or a limited number of) point source(s). On the contrary, the residuals of the multiscale algorithm are closer to zero on average. Therefore, we chose the multiscale algorithm for all of the [C II]$_{158\ \mu m}$-derived quantities and images in this paper.

Figure 14 shows the clean, dirty, and residual maps for the continuum maps and the other FSL maps for a Högbom clean. For the lower-frequency continuum maps, the [O I]$_{146\ \mu m}$ maps, and the [N II]$_{205\ \mu m}$ maps, the residuals are well-behaved and do not require the use of multiscale cleaning. For the 259 and 274 GHz continuum maps, some residuals are seen, and the multiscale algorithm is adopted for those in the paper, albeit changing only the final continuum flux by $\lesssim$2%.

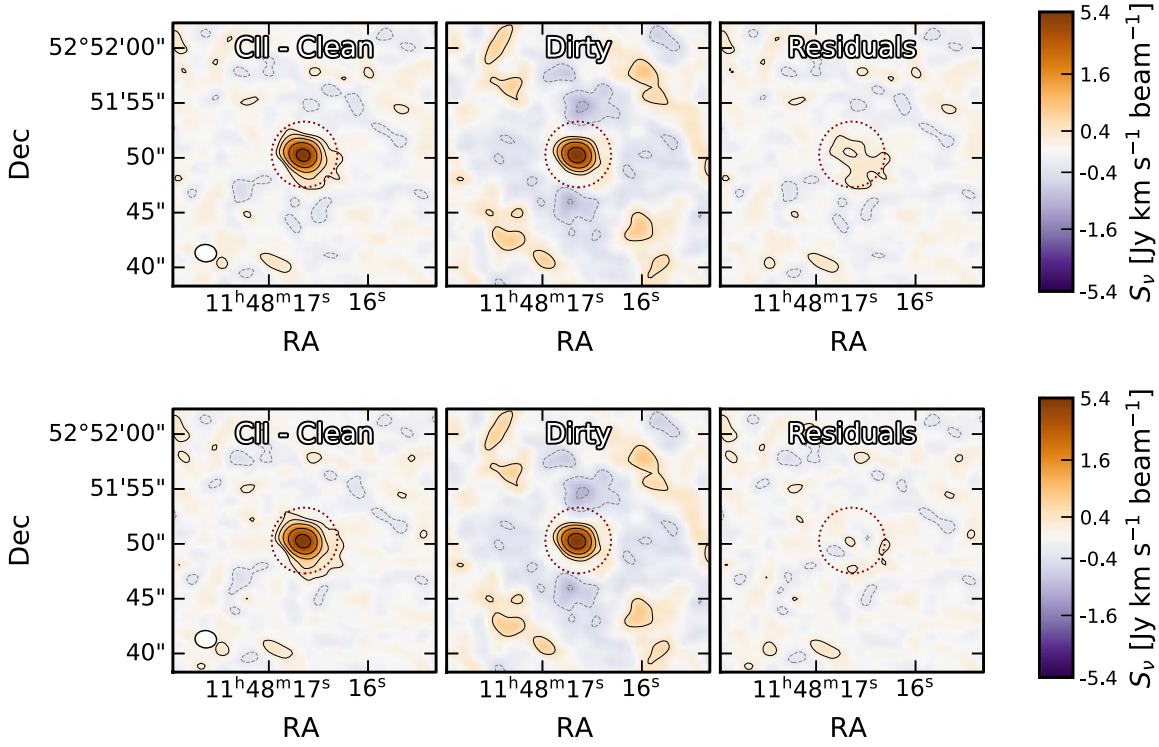


Figure 13. Clean, dirty, and residual maps of the [C II]$_{158\ \mu m}$ emission for two different cleaning algorithms: Högbom (the first row) and multiscale (the second row). Both are cleaned down to 2σ, where σ is the rms noise of the dirty map.

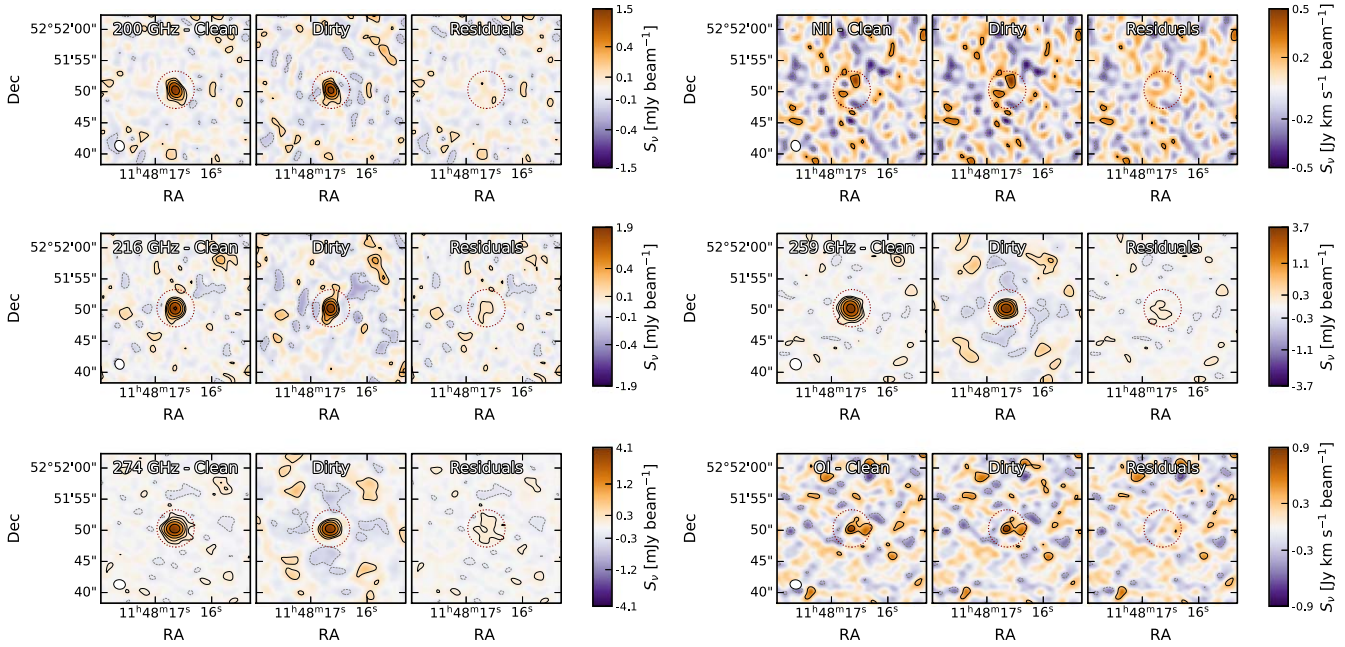


Figure 14. Clean, dirty, and residual maps for a Högbom clean to 2σ of the 200 GHz continuum, $[\mathrm{N\ II}]_{205\ \mu\mathrm{m}}$ emission, the 216, 259, and 274 GHz continua, and finally the $[\mathrm{O\ I}]_{146\ \mu\mathrm{m}}$ emission.

Appendix C
Dust SED Parameter Posterior Distribution

We present in Figure 15 the posterior distribution of the dust SED parameters fitted in Section 2. The median dust properties derived are consistent with the existing literature on high-redshift quasars (e.g., Venemans et al. 2020).

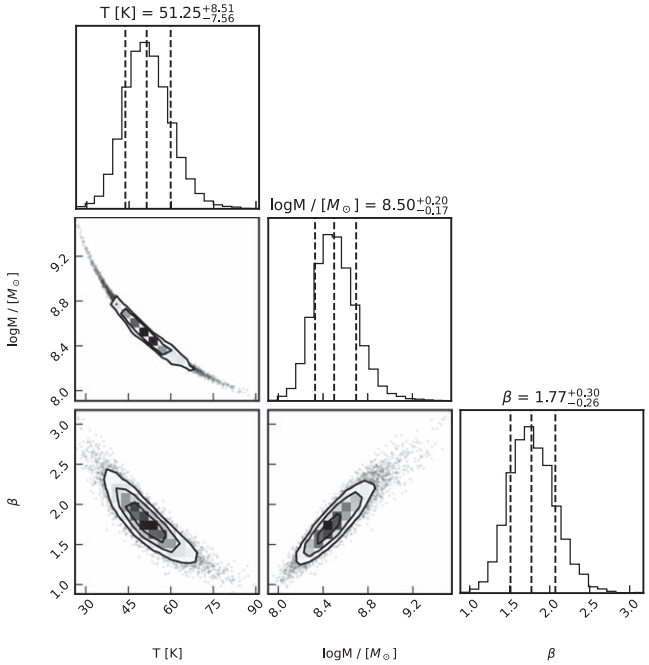


Figure 15. The dust SED–fitting posterior distribution of the dust temperature T, dust mass M, and the dust spectral emissivity index β.

Appendix D
[C II]$_{158\ \mu m}$ Flux Density

In Table 3, we compare the [C II]$_{158\ \mu m}$ fluxes measured from the extracted aperture-integrated [C II]$_{158\ \mu m}$ spectra for various aperture sizes between previous studies and this work. This work's spectra and best-fit Gaussians are displayed in Figure 16 for circular apertures with radii $r = 1''$, $2''$, and $4''$, and a central-pixel-only spectrum. The $r = 3''$ case has already been presented in the main text (Figure 5). For Cicone et al. (2015), we report their best-fit parameters and fluxes for the "narrow" (-200, 200) km s^{-1} component defined in their study. We find good agreement for all apertures between this work and previous studies. This implies that most of the excess flux in larger apertures ($r \gtrsim 3''$) described in Cicone et al. (2015) is due to the reported presence of blue-/redshifted components with large spatial offsets that are not recovered in this work, as discussed in Section 4.

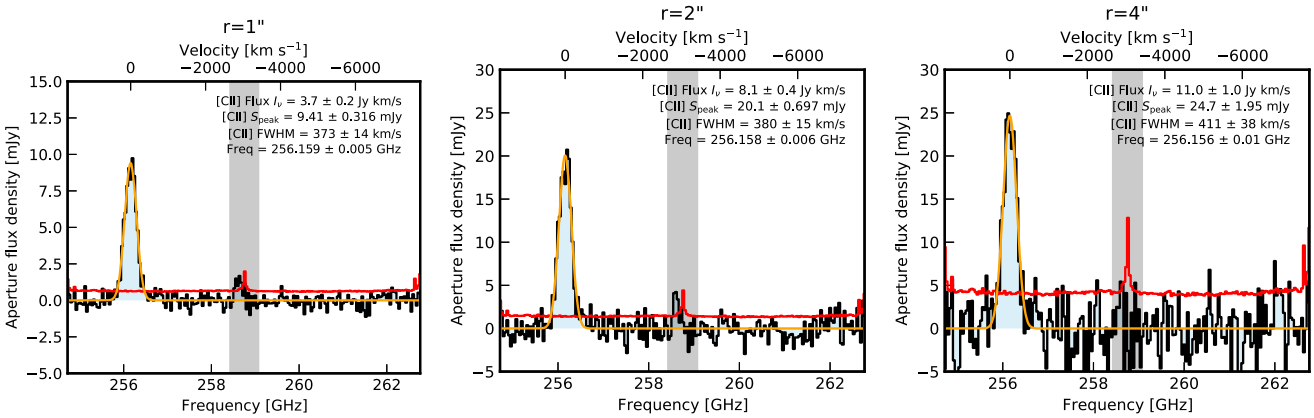


Figure 16. Continuum-subtracted aperture-integrated [C II]$_{158\ \mu m}$ spectra (black) for circular apertures with radii $r = 1''$, $2''$, and $4''$. The best-fit Gaussian is shown in orange, and the best-fit parameters are displayed in the upper right corners of each plot.

Table 3
[C II]$_{158\ \mu m}$ Line Fluxes Measured from a Gaussian Fit to the Aperture-integrated Spectra in This Work and Previous Studies

	$r = 1''$		$r = 2''$		$r = 3''$		$r = 4''$	
	Cicone et al. (2015)	This work	Cicone et al. (2015)	This work	Maiolino et al. (2012)	This work	Cicone et al. (2015)	This work
σ_v [km s^{-1}]	146 ± 11	158 ± 6	148 ± 16	162 ± 4	150 ± 20	171 ± 10	150 ± 20	175 ± 16
S_{peak} [mJy]	14.5 ± 0.9	9.41 ± 0.32	30 ± 3	20.1 ± 0.7	23 ± 2	23.5 ± 1.2	34 ± 4	24.7 ± 2.0
I_ν [Jy km s^{-1}]	5.3 ± 0.5	3.7 ± 0.2	11.0 ± 1.5	8.1 ± 0.4	14 ± 3	10.0 ± 0.8	13 ± 3	11.0 ± 1.0

Note. For each aperture radius and study, we give the best-fit velocity width σ_v, the peak line flux density S_{peak}, and the integrated flux I_ν. For the Cicone et al. (2015) values, only the narrow-component results ([C II]$_{158\ \mu m}$ emission integrated between (-200, 200) km s^{-1}) are reported. The Walter et al. (2009a) best-fit values are: $\sigma_v = 122 \pm 12$ km s^{-1}, $S_{peak} = 12.7 \pm 1.1$ mJy, and $I_\nu = 3.9 \pm 0.3$ Jy km s^{-1}. Similarly, the Maiolino et al. (2005) IRAM 30 m measurement gives: $\sigma_v = 149 \pm 21$ km s^{-1}, $S_{peak} = 11.8$ mJy, and $I_\nu = 4.1 \pm 0.5$ Jy km s^{-1}.

Appendix E
Continuum Subtraction and Masking of the [C II]$_{158\ \mu m}$ Line

In this appendix, we provide details about the continuum subtraction procedures, focusing on the [C II]$_{158\ \mu m}$ spectral setup. Figure 17 shows the aperture-integrated [C II]$_{158\ \mu m}$ spectrum for various half-width masking regions, ranging from $4.5 \times \mathrm{FWHM([C\,II])} = 1733$ km s^{-1} to $0.5 \times \mathrm{FWHM([C\,II])} = 193$ km s^{-1}. In all cases, we fit single- and double-Gaussian models to the [C II]$_{158\ \mu m}$ emission (as in Section 4.1)

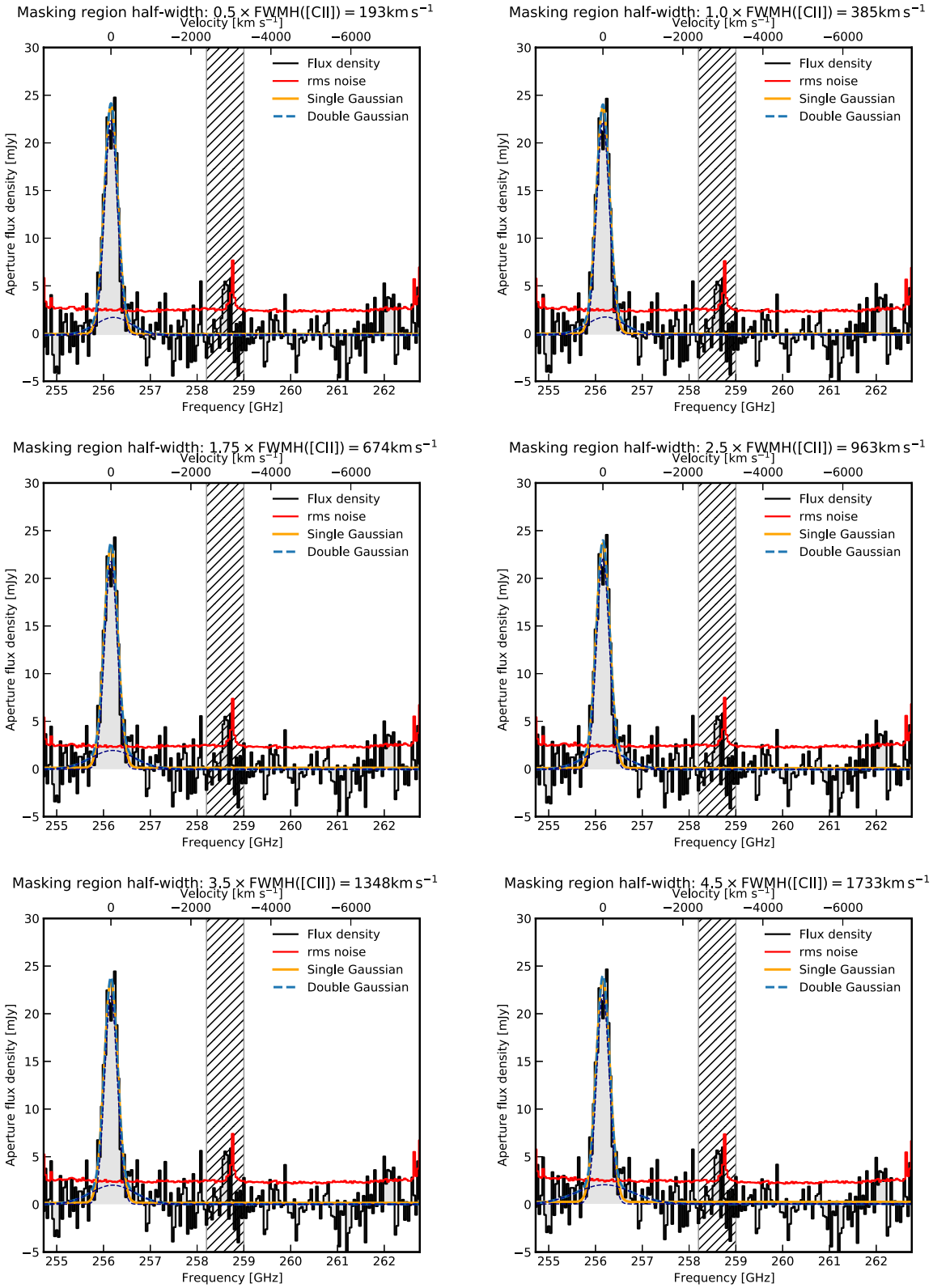


Figure 17. Spectra of the [C II]$_{158\ \mu m}$ line for different continuum subtractions. The line half-width masking region is indicated in the title of each panel. The colors and symbols are the same as in Figure 5.

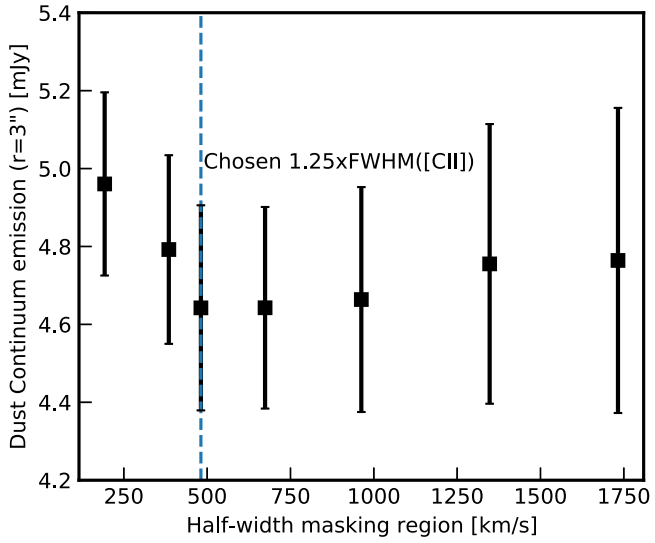


Figure 18. Aperture-integrated continuum flux density at 259 GHz as a function of the line masking half-width. The measurement has converged at the adopted masking width of 1.25 × FWHM([C II]).

and find no evidence to reject the single-Gaussian model in favor of a double-Gaussian emission profile. Finally, Figure 18 shows the dust continuum measurement as a function of the masking half-width. The continuum is predictably higher for small masking regions, but has converged at the masking half-width adopted in this paper (1.25 × FWHM([C II])).

Appendix F
Previous PdBI Data and Merge with the New NOEMA Data

In this appendix, we analyze the previous PdBI observations of J1148+5251 published in Cicone et al. (2015). We do not recalibrate their data, and we follow our analysis method as presented in Sections 2 and 3. Based on the previous PdBI data, we show the total spectrum extracted in a $r = 3''$ aperture, applying residual scaling corrections (e.g., Jorsater & van Moorsel 1995; Walter & Brinks 1999; Walter et al. 2008; Novak et al. 2019), in Figure 19 (where we also show the new NOEMA spectrum for comparison). Clearly, the two data sets are compatible, and a single-Gaussian+continuum fit gives similar continuum levels and $[\mathrm{C\,II}]_{158\ \mu\mathrm{m}}$ peak fluxes within the ∼10%–20% amplitude calibration errors. We note that the noise in the previous PdBI spectrum is not uniform, as different data sets with different frequency coverages and antenna configurations were stitched together (Cicone et al. 2015). This leads to increased noise in the ranges $\nu \lesssim 254.7$ GHz and $\nu \gtrsim 258.0$ GHz. The best-fit continuum to the total spectrum in $r = 3''$ (4.6 ± 0.3 mJy) is perfectly consistent with the new measurement (4.5 ± 0.2 mJy) and the best-fit dust SED (Section 3.1), and in tension with the 3.3 mJy continuum value (at 256 GHz) published in Cicone et al. (2015), derived from a best-fit model in the UV plane to line-free channels. We therefore infer that this tension is probably due to an unfortunate choice of continuum channels or an unstable UV plane–fitting routine in the old pipeline.

We then show in Figure 20 different spectra extracted from the previous PdBI data set with and without residual scaling. It can be clearly seen that the continuum flux at the edges of the band drops significantly in larger apertures when residual scaling is not used. This subtle effect is due to the fact that the continuum is only detected at the $\lesssim 2\sigma$ level in most line-free channels (e.g., at the edges of the band). When cleaning down to a typical 2σ threshold, there is in fact no or little flux above that threshold, and therefore no or few clean components are added to the final "clean" map (which is the sum of the clean Gaussian components and the residual map that does not have "clean beam" but "dirty beam" units) for channels that only contain continuum emission. As a consequence, these channels are dominated by the residual map that imprints the dirty beam pattern. With large apertures, e.g., $r > 3''$ in this case, one starts to integrate over negative sidelobes of the synthesized beam, decreasing the integrated flux significantly. This effect does not play a dominant role where the $[\mathrm{C\,II}]_{158\ \mu\mathrm{m}}$ line is present, since in those channels the flux is dominated by the actual "clean" components. This can then lead, when combined with an undersubtracted continuum, to the illusion of a strong broad component in the final spectrum. However, with the residual scaling approach taken into account, this broad component is less significant (although still tentatively detected; see Figure 21), and the results become compatible with the new NOEMA data.

We now comment on the $[\mathrm{C\,II}]_{158\ \mu\mathrm{m}}$ structure reported in Cicone et al. (2015). We show in Figure 22 the collapsed $[\mathrm{C\,II}]_{158\ \mu\mathrm{m}}$ channels in the range of $(-1400, +1200)$ km s^{-1} based on the previous PdBI data only. We find a similar structure as previously reported, but at a different significance level (in our case, not exceeding the 3σ level in the extended regions). We therefore speculate that the rms might have been underestimated by the earlier GILDAS/MAPPING software release, which would explain the numerous -6 and -3σ regions in the previously published $[\mathrm{C\,II}]_{158\ \mu\mathrm{m}}$ map.

We conclude this appendix by presenting the results of our analysis of the merged PdBI and NOEMA $[\mathrm{C\,II}]_{158\ \mu\mathrm{m}}$ spectra. We show in Figure 23 the total and continuum-subtracted spectra of the merged $[\mathrm{C\,II}]_{158\ \mu\mathrm{m}}$ data. Although the statistical analysis of the spectrum extracted from this combined data set continues to prefer a single-component fit, there is evidence for the detection of a small flux excess in the redshifted $[\mathrm{C\,II}]_{158\ \mu\mathrm{m}}$ line wing that might indicate the presence of weak outflow or an unresolved companion as in J0305–3150 (see Venemans et al. 2017a, 2019).

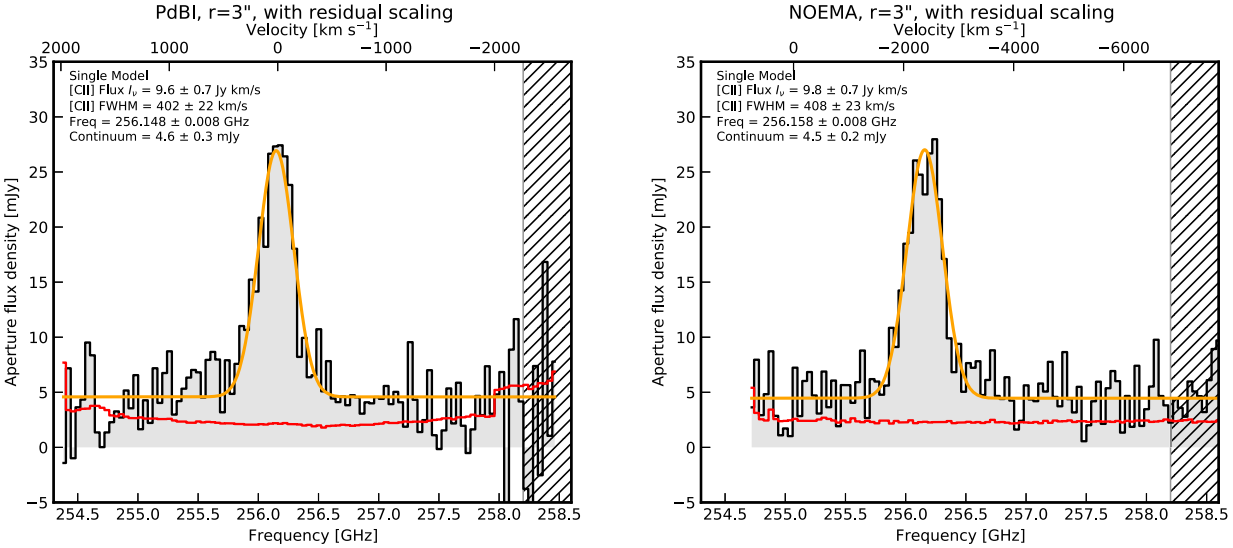


Figure 19. The total spectrum (black) of the [C II]$_{158\ \mu m}$ line, extracted in $r = 3''$ apertures, using residual scaling, in the previous PdBI data (left) and the new NOEMA data (right). The single-Gaussian (+continuum) fits to both data sets are shown in orange, and the parameters are given in the upper left corners. The best-fit continuum (constant) and single-Gaussian model parameters are consistent between the two data sets. We note that the increases in noise (shown as the red lines) in the PdBI data at low (<254.7 GHz) and high (>258 GHz) frequencies are due to the way in which the data were frequency-stitched at the time.

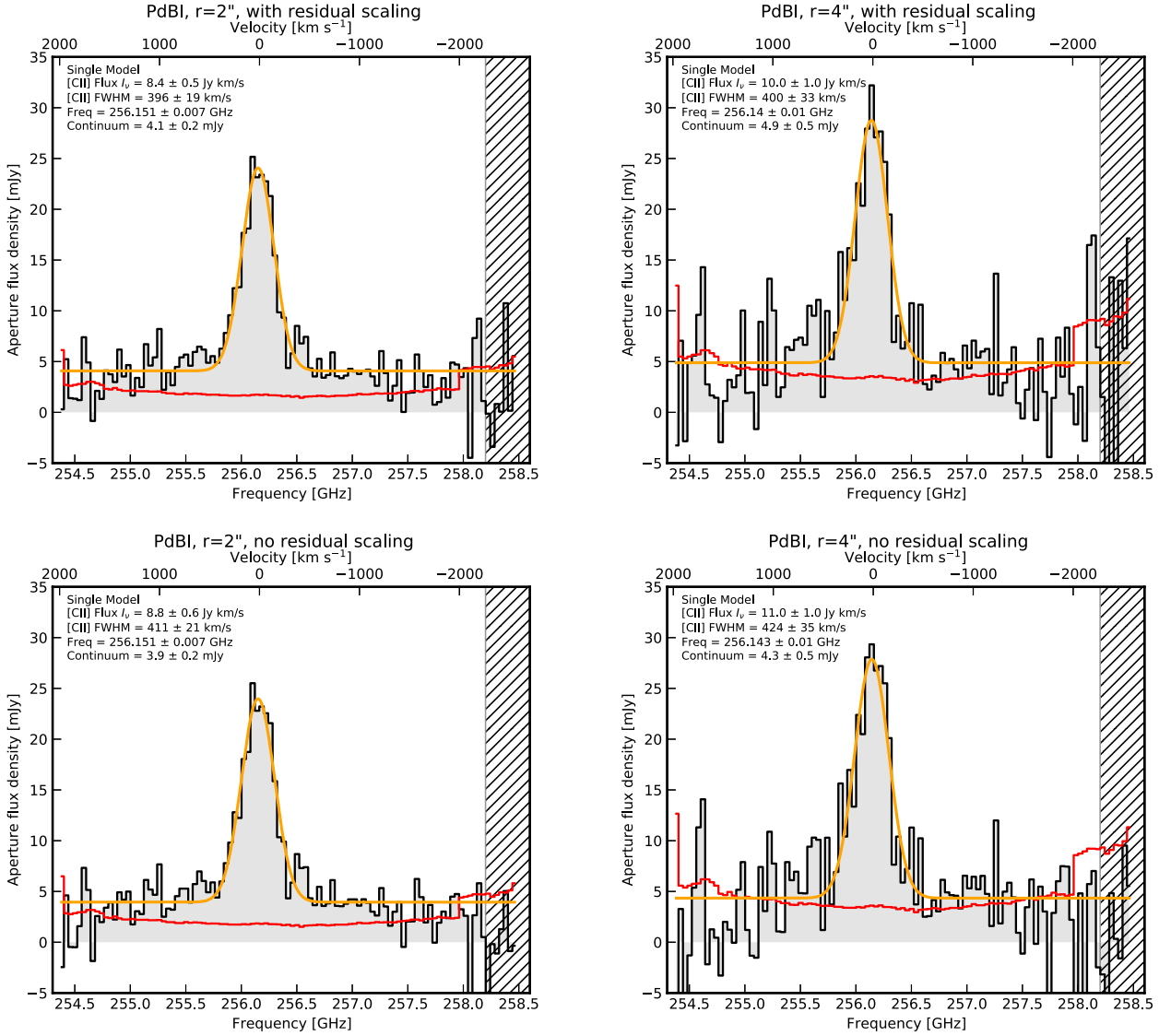


Figure 20. The total spectra of the [C II]$_{158\ \mu m}$ line, with (first row) and without (second row) residual scaling, extracted in $r = 2''$ and $r = 4''$ apertures (the first and second columns, respectively), in the PdBI data. The single-Gaussian (+continuum) fits to both data sets are shown in orange. In the absence of residual scaling, the continuum flux drops away from the [C II]$_{158\ \mu m}$ line in the larger apertures (see the text for details). Even though no continuum was subtracted in the UV plane, the continuum flux approaches ~ 0 mJy at the band edges in the $r = 4''$ aperture (without residual scaling), creating the illusion of a broad emission line.

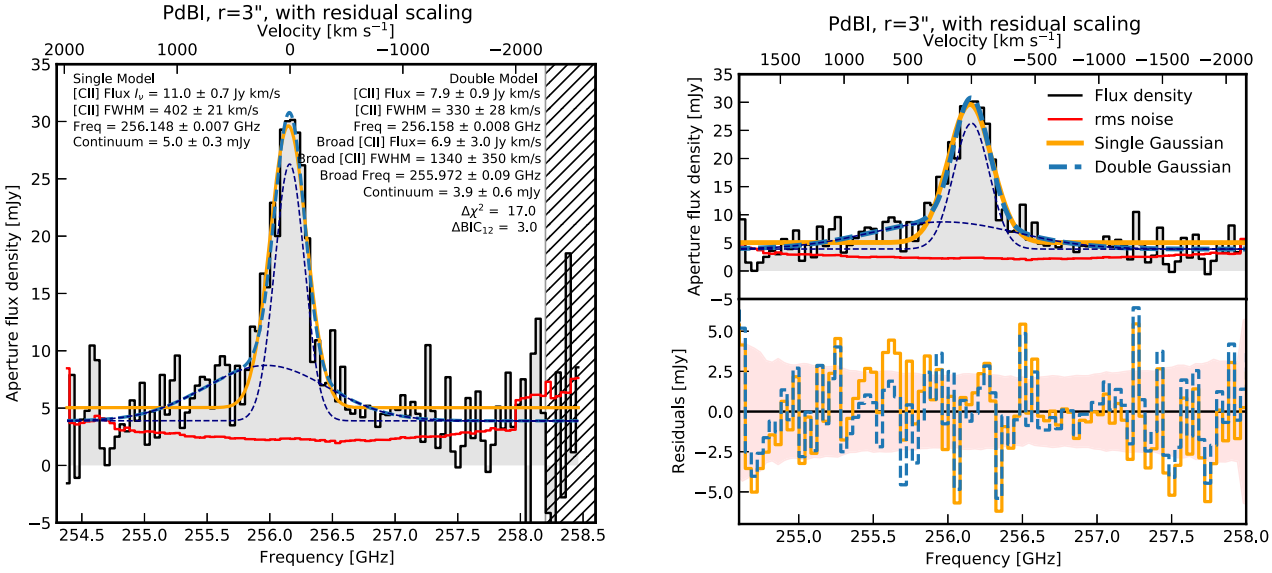


Figure 21. The total spectrum of the [C II]$_{158\ \mu m}$ line (black), presented as in Figure 5, but using the previous PdBI data, following the methodology used in this paper. Both the single-Gaussian and double-Gaussian fits are consistent with those performed on the NOEMA data only (see Figure 5). With ΔBIC$_{12} = 3.0 < 10$, a broad [C II]$_{158\ \mu m}$ component is only tentatively detected.

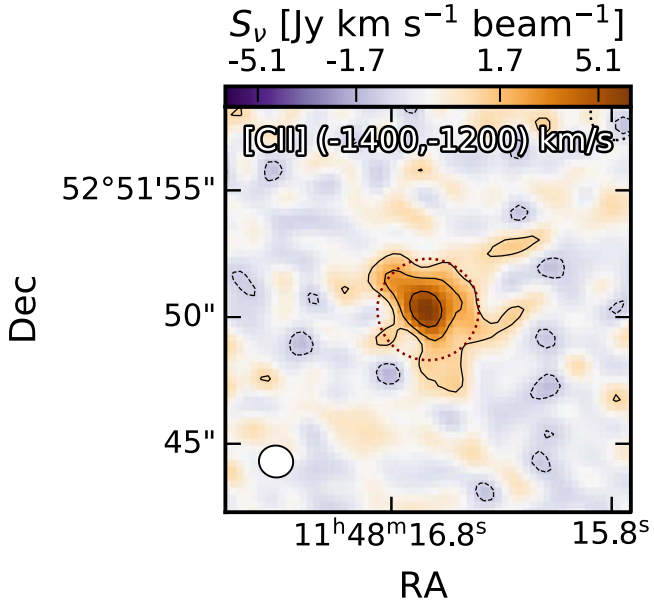


Figure 22. [C II]$_{158\ \mu m}$ line map integrated over (− 1400, + 1200) km s^{-1} using the previous PdBI data. The (dashed) black contours are at the (− 2, 2, 4, 8)σ level, where σ is the rms computed directly from the map with σ-clipping. The extended [C II]$_{158\ \mu m}$ structure reported in Cicone et al. (2015) is recovered, albeit at a lower significance level (see the main text for details).

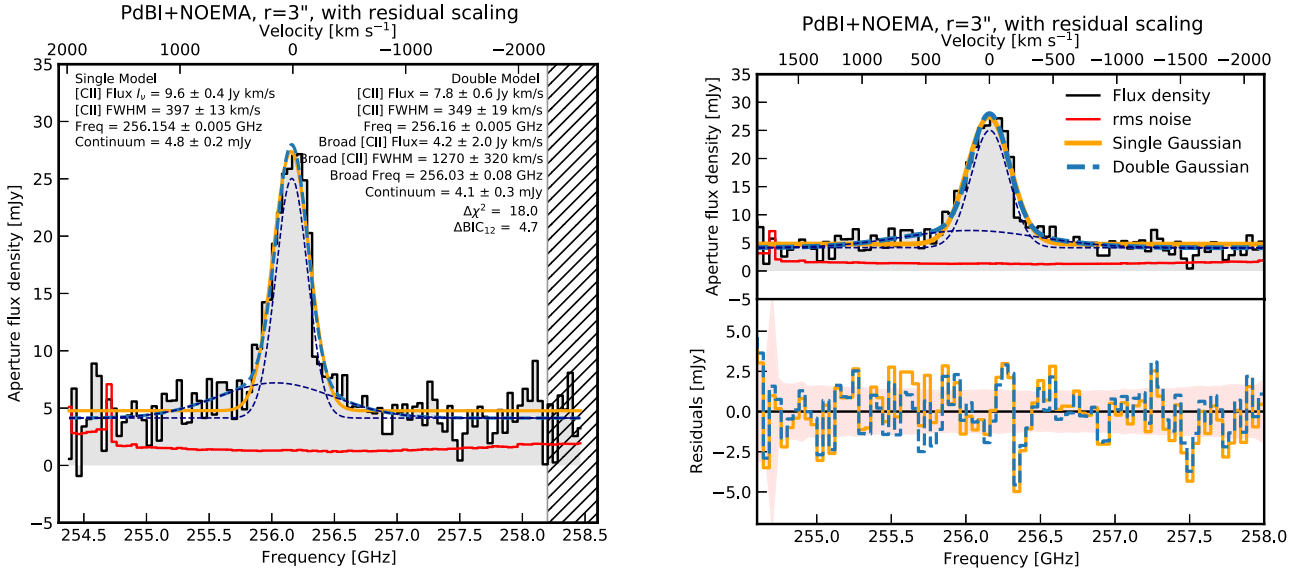


Figure 23. The total spectrum of the [C II]$_{158\ \mu m}$ line (black), presented as in Figure 5, but using the merged PdBI and NOEMA data set. Both the single-Gaussian and double-Gaussian fits are consistent with those performed on the NOEMA data only (see Figure 5). With ΔBIC$_{12} = 4.7 < 10$, a broad [C II]$_{158\ \mu m}$ component is only tentatively detected in the merged PdBI and NOEMA data set.

Appendix G
Channel and Moment Maps of the [C II]$_{158\ \mu m}$ Emission

In this appendix, we present additional visualizations of the [C II]$_{158\ \mu m}$ emission velocity structure in J1148+5251. First, we present channel maps in Figure 24 with a channel width of 117 km s^{-1}. No significant emission ($>3\sigma$) is detected at large radii or at velocity offsets >400 km s^{-1} from the peak of the [C II]$_{158\ \mu m}$ line (see Cicone et al. 2015). Second, we present the integrated flux, mean velocity, and velocity dispersion (so-called moment maps) in Figure 25. These maps are generated using *Qubefit* (Neeleman et al. 2020) using all [C II]$_{158\ \mu m}$ voxels detected at S/N > 3 and standard parameters. We find no kinematic evidence for a bulge-dominated dispersion or a rotating disk model.

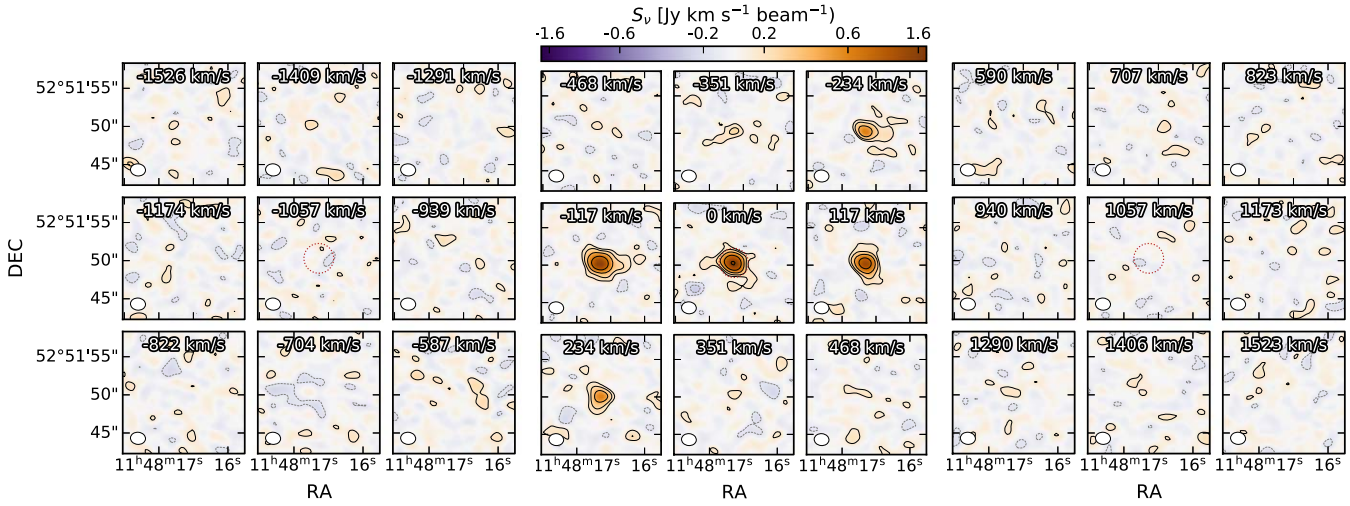


Figure 24. Channel map of the [C II]$_{158\ \mu m}$ line of J1148+5251, in channels of 117 km s^{-1}. The contours are logarithmic ($-8, -4, -2, 2, 4, 8, 16, 32$)$\sigma$ (rms). The color scaling is log-linear, the threshold being at 3σ (rms).

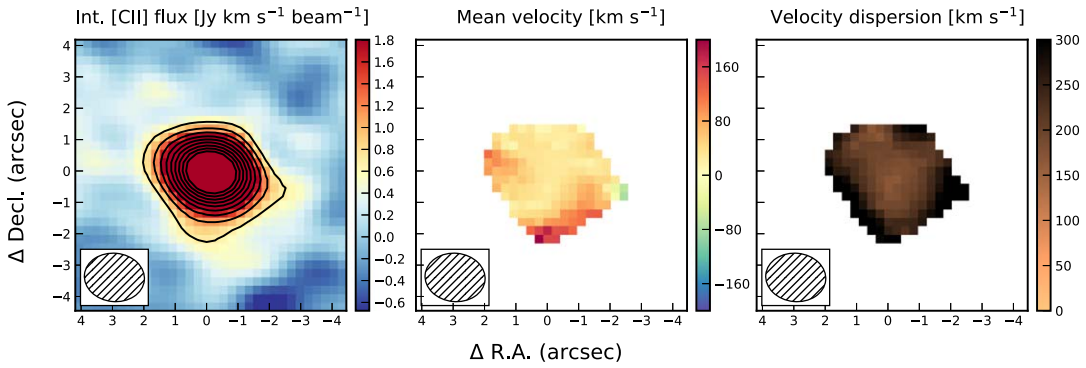


Figure 25. Moment maps of the [C II]$_{158\ \mu m}$ emission. The integrated velocity and velocity dispersion are only shown in pixels at the 3σ level. The absence of any velocity structure is expected, given that the 3σ detected area covers only ∼4 beams.

ORCID iDs

Romain A. Meyer https://orcid.org/0000-0001-5492-4522
Fabian Walter https://orcid.org/0000-0003-4793-7880
Claudia Cicone https://orcid.org/0000-0003-0522-6941
Pierre Cox https://orcid.org/0000-0003-2027-8221
Roberto Decarli https://orcid.org/0000-0002-2662-8803
Roberto Neri https://orcid.org/0000-0002-7176-4046
Mladen Novak https://orcid.org/0000-0001-8695-825X
Antonio Pensabene https://orcid.org/0000-0001-9815-4953
Dominik Riechers https://orcid.org/0000-0001-9585-1462
Axel Weiss https://orcid.org/0000-0003-4678-3939

References

Bañados, E., Decarli, R., Walter, F., et al. 2015, ApJL, 805, L8
Bañados, E., Venemans, B. P., Mazzucchelli, C., et al. 2018, Natur, 553, 473
Beelen, A., Cox, P., Benford, D. J., et al. 2006, ApJ, 642, 694
Bertoldi, F., Carilli, C. L., Cox, P., et al. 2003a, A&A, 406, L55
Bertoldi, F., Cox, P., Neri, R., et al. 2003b, A&A, 409, L47
Bischetti, M., Maiolino, R., Carniani, S., et al. 2019, A&A, 630, A59
Boogaard, L., Meyer, R. A., & Novak, M. 2021, Interferopy: Analyzing Data Cubes from Radio-to-submm Observations, Zenodo, doi:10.5281/ZENODO.5775603
Bosman, S. E. I. 2020, All z>5.7 quasars currently known v1.15 Zenodo, doi:10.5281/zenodo.6039724
Brauher, J. R., Dale, D. A., & Helou, G. 2008, ApJS, 178, 280
Carilli, C., & Walter, F. 2013, ARA&A, 51, 105
Cicone, C., Maiolino, R., Gallerani, S., et al. 2015, A&A, 574, 14
Cicone, C., Maiolino, R., Sturm, E., et al. 2014, A&A, 562, A21
Costa, T., Sijacki, D., & Haehnelt, M. G. 2014, MNRAS, 444, 2355
Croxall, K. V., Smith, J. D., Pellegrini, E., et al. 2017, ApJ, 845, 96
Da Cunha, E., Groves, B., Walter, F., et al. 2013, ApJ, 766, 13
De Breuck, C., Weiß, A., Béthermin, M., et al. 2019, A&A, 631, A167
De Looze, I., Cormier, D., Lebouteiller, V., et al. 2014, A&A, 568, A62
De Rosa, G., Venemans, B. P., Decarli, R., et al. 2014, ApJ, 790, 145
Decarli, R., Dotti, M., Bañados, E., et al. 2019a, ApJ, 880, 157
Decarli, R., Mignoli, M., Gilli, R., et al. 2019b, A&A, 631, L10
Decarli, R., Walter, F., Carilli, C., et al. 2014, ApJ, 782, 78
Decarli, R., Walter, F., Venemans, B. P., et al. 2018, ApJ, 854, 97
Di Matteo, T., Springel, V., & Ilernquist, L. 2005, Natur, 433, 604
Díaz-Santos, T., Armus, L., Charmandaris, V., et al. 2017, ApJ, 846, 32
Dunne, L., Eales, S. A., & Edmunds, M. G. 2003, MNRAS, 341, 589
Fan, X., Strauss, M. A., Schneider, D. P., et al. 2003, AJ, 125, 1649
Ferkinhoff, C., Brisbin, D., Nikola, T., et al. 2011, ApJL, 740, 29
Ferkinhoff, C., Hailey-Dunsheath, S., Nikola, T., et al. 2010, ApJL, 714, 147
Ferland, G. J., Chatzikos, M., Guzmán, F., et al. 2017, The 2017 Release of Cloudy, Zenodo, doi:10.5281/zenodo.4110791
Fernández-Ontiveros, J. A., Spinoglio, L., Pereira-Santaella, M., et al. 2016, ApJS, 226, 19
Foreman-Mackey, D., Hogg, D. W., Lang, D., & Goodman, J. 2013, PASP, 125, 306
Fujimoto, S., Ouchi, M., Ferrara, A., et al. 2019, ApJ, 887, 107
Fujimoto, S., Silverman, J. D., Bethermin, M., et al. 2020, ApJ, 900, 1
Gallerani, S., Ferrara, A., Neri, R., & Maiolino, R. 2014, MNRAS, 445, 2848
Gullberg, B., De Breuck, C., Vieira, J. D., et al. 2015, MNRAS, 449, 2883
Harris, C. R., Jarrod Millman, K., van der Walt, S. J., et al. 2020, Natur, 585, 357
Hashimoto, T., Inoue, A. K., Tamura, Y., et al. 2019, PASJ, 71, 71
Helou, G., Soifer, B. T., & Rowan-Robinson, M. 1985, ApJL, 298, L7
Herrera-Camus, R., Bolatto, A., Smith, J. D., et al. 2016, ApJ, 826, 175
Herrera-Camus, R., Schreiber, N. F., Genzel, R., et al. 2021, A&A, 649, A31
Herrera-Camus, R., Sturm, E., Graciá-Carpio, J., et al. 2018a, ApJ, 861, 94
Herrera-Camus, R., Sturm, E., Graciá-Carpio, J., et al. 2018b, ApJ, 861, 95
Högbom, J. A. 1974, A&AS, 15, 417
Hunter, J. D. 2007, CSE, 9, 90
Ishibashi, W., & Fabian, A. C. 2015, MNRAS, 451, 93
Izumi, T., Matsuoka, Y., Fujimoto, S., et al. 2021a, ApJ, 914, 36
Izumi, T., Onoue, M., Matsuoka, Y., et al. 2021b, ApJ, 908, 235
Jorsater, S., & van Moorsel, G. A. 1995, AJ, 110, 2037
Kass, R. E., & Raftery, A. E. 1995, J. Am. Stat. Assoc., 90, 773
Katz, H., Kimm, T., Haehnelt, M. G., et al. 2019, MNRAS, 483, 1029
Katz, H., Kimm, T., Sijacki, D., & Haehnelt, M. G. 2017, MNRAS, 468, 4831
Kennicutt, R. C. 1998, ARA&A, 36, 189
Kennicutt, R. C., & Evans, N. J. 2012, ARA&A, 50, 531
King, A. R. 2010, MNRAS Lett., 408, L95
Koudmani, S., Henden, N. A., & Sijacki, D. 2021, MNRAS, 503, 3568
Lagache, G., Cousin, M., & Chatzikos, M. 2018, A&A, 609, 130
Lee, M. M., Nagao, T., De Breuck, C., et al. 2021, ApJ, 913, 41
Leipski, C., Meisenheimer, K., Klaas, U., et al. 2010, A&A, 518, L34
Leipski, C., Meisenheimer, K., Walter, F., et al. 2014, ApJ, 785, 154
Li, J., Wang, R., Cox, P., et al. 2020, ApJ, 900, 131
Maiolino, R., Cox, P., Caselli, P., et al. 2005, A&A, 440, 51
Maiolino, R., Gallerani, S., Neri, R., et al. 2012, MNRAS, 425, L66
Mazzucchelli, C., Bañados, E., Venemans, B. P., et al. 2017, ApJ, 849, 91
Neeleman, M., Bañados, E., Walter, F., et al. 2019, ApJ, 882, 10
Neeleman, M., Novak, M., Venemans, B. P., et al. 2021, ApJ, 911, 141
Neeleman, M., Prochaska, J. X., Kanekar, N., et al. 2020, qubefit: MCMC kinematic modeling, Astrophysics Source Code Library, ascl:2005.013
Negri, A., & Volonteri, M. 2017, MNRAS, 467, 3475
Neri, R., Downes, D., Cox, P., & Walter, F. 2014, A&A, 562, 35
Novak, M., Bañados, E., Decarli, R., et al. 2019, ApJ, 881, 63
Novak, M., Venemans, B. P., Walter, F., et al. 2020, ApJ, 904, 131
Oberst, T. E., Parshley, S. C., Stacey, G. J., et al. 2006, ApJL, 652, L125
Oppenheimer, B. D., Davies, J. J., Crain, R. A., et al. 2020, MNRAS, 491, 2939
Pavesi, R., Riechers, D. A., Capak, P. L., et al. 2016, ApJ, 832, 151
Pavesi, R., Riechers, D. A., Faisst, A. L., Stacey, G. J., & Capak, P. L. 2019, ApJ, 882, 168
Pensabene, A., Decarli, R., Bañados, E., et al. 2021, A&A, 652, A66
Richardson, M. L. A., Scannapieco, E., Devriendt, J., et al. 2016, ApJ, 825, 83
Riechers, D. A., Walter, F., Bertoldi, F., et al. 2009, ApJ, 703, 1338
Robson, I., Priddey, R. S., Isaak, K. G., & McMahon, R. G. 2004, MNRAS, 351, L29
Savage, B. D., & Sembach, K. R. 1996, ARA&A, 34, 279
Shao, Y., Wang, R., Carilli, C. L., et al. 2019, ApJ, 876, 99
Shao, Y., Wang, R., Jones, G. C., et al. 2017, ApJ, 845, 138
Silk, J., & Rees, M. J. 1998, A&A, 331, L1
Solomon, P. M., Downes, D., Radford, S. J. E., & Barrett, J. W. 1997, ApJ, 478, 144
Springel, V., Di Matteo, T., & Hernquist, L. 2005, MNRAS, 361, 776
The Astropy Collaboration, Price-Whelan, A. A. M., Sipocz, B. M., et al. 2018, AJ, 156, 19

Vallini, L., Gallerani, S., Ferrara, A., Pallottini, A., & Yue, B. 2015, ApJ, 813, 36
Venemans, B., Neeleman, M., Walter, F., et al. 2019, ApJL, 874, L30
Venemans, B. P., Decarli, R., Walter, F., et al. 2018, ApJ, 866, 159
Venemans, B. P., Walter, F., Decarli, R., et al. 2017a, ApJL, 851, L8
Venemans, B. P., Walter, F., Decarli, R., et al. 2017b, ApJ, 837, 146
Venemans, B. P., Walter, F., Neeleman, M., et al. 2020, ApJ, 904, 130
Virtanen, P., Gommers, R., Oliphant, T. E., et al. 2020, NatMe, 17, 261
Wakker, B. P., & Schwarz, U. J. 1988, A&A, 200, 312
Walter, F., Bertoidl, F., Carilli, C., et al. 2003, Natur, 424, 406
Walter, F., & Brinks, E. 1999, AJ, 118, 273
Walter, F., Brinks, E., de Blok, W. J. G., et al. 2008, AJ, 136, 2563
Walter, F., Carilli, C., Bertoldi, F., et al. 2004, ApJL, 615, L17
Walter, F., Riechers, D., Cox, P., et al. 2009a, Natur, 457, 699
Walter, F., Riechers, D., Novak, M., et al. 2018, ApJL, 869, L22
Walter, F., Wei, A., Riechers, D. A., et al. 2009b, ApJ, 691, L1
Wang, F., Yang, J., Fan, X., et al. 2021, ApJL, 907, L1
Wang, R., Shao, Y., Carilli, C. L., et al. 2019, ApJ, 887, 40
Wang, R., Wagg, J., Carilli, C. L., et al. 2013, ApJ, 773, 44
Weiß, A., Henkel, C., Downes, D., & Walter, F. 2003, A&A, 409, L41
Weiß, A., Downes, D., Henkel, C., & Walter, F. 2005, A&A, 429, L25
Willott, C. J., McLure, R. J., & Jarvis, M. J. 2003, ApJL, 587, L15
Yang, J., Venemans, B., Wang, F., et al. 2019, ApJ, 880, 153
Yang, J., Wang, F., Fan, X., et al. 2020, ApJL, 897, L14
Zhao, Y., Lu, N., Xu, C. K., et al. 2016, ApJ, 819, 69